

Highlights

Coherent pulse interactions in mode-locked semiconductor lasers

Thomas G. Seidel, Julien Javaloyes, Svetlana V. Gurevich

- Equations of motion for interacting mode-locked pulses
- Temporal localized states
- Bifurcation analysis
- Time-delayed feedback

Coherent pulse interactions in mode-locked semiconductor lasers

Thomas G. Seidel^a, Julien Javaloyes^c and Svetlana V. Gurevich^{a,b,*}

^aInstitute for Theoretical Physics, University of Münster, Wilhelm-Klemm-Str. 9, Münster, 48149, Germany

^bCenter for Nonlinear Science (CeNoS), University of Münster, Corrensstrasse 2, Münster, 48149, Germany

^cDepartament de Física, Universitat de les Illes Balears, & Institute of Applied Computing and Community Code (IAC-3), C/ Valldemossa km 7.5, Mallorca, 07122, Spain

ARTICLE INFO

Keywords:

Passive Mode-Locking
Frequency Combs
Bifurcation analysis

ABSTRACT

We study the dynamics of multipulse solutions in mode-locked lasers in presence of time-delayed feedback stemming, e.g., from reflections upon optical elements, and carrier dynamics. We demonstrate that the dynamics of such a high dimensional problem can be successfully described by some effective equations of motion for the pulses' phases and positions. Analyzing the reduced vector field permits disclosing a highly complex dynamics where coherent and incoherent interactions compete. The latter lead to regimes in which pulses can be equidistant or non-equidistant and also have different phase relations. Multi-stability between regimes is also observed as well as emerging limit cycles and global heteroclinic bifurcations in the reduced phase space.

Mode-locking (ML) is a well-established method for achieving ultrashort optical pulses with high repetition rates [1] and optical frequency combs [2, 3, 4] which has proven to be highly relevant for a variety of applications ranging from metrology to medical imaging, see e.g., [5, 6, 7, 8, 9, 10, 11, 12]. Among other ML techniques, passive mode-locking is achieved by combining two elements, a laser amplifier providing gain and a nonlinear loss element, usually a saturable absorber. It was shown [13] that when a passive mode-locked laser is operated in the long-cavity regime in which the cavity round-trip is much larger than the gain recovery time, the optical pulses become individually addressable temporally localized structures coexisting with the off solution [14, 15, 16]. There, a very large number of solutions with different number of pulses per round-trip and different arrangement become multistable. Besides the fundamental mode-locked regime where a single pulse circulates in the laser cavity, a mode-locked laser can be operated in the harmonic mode-locked regime where the laser cavity supports a train of several pulses within one round-trip. The gain depletion and subsequent recovery in an harmonic mode-locked laser provides an effective repulsion force leading to the formation of a regime with equally spaced pulses [17, 18, 19]. However, even in this ordered state, it was recently demonstrated that the many pulses emitted by an harmonically mode-locked laser are not necessarily coherent with each other [20]; The derived effective equations of motion (EOM) for the phase differences of the neighbouring pulses indicated that the ensemble behaves like coupled oscillators which have multiple equilibria that can be linked to the splay states of the Kuramoto model with short range interactions.

The current manuscript discusses how minute optical feedback stemming from parasitic elements such as intracavity lenses or from an external mirror can drastically

modify the emission of passively mode-locked lasers in the multi-pulse regimes observed in the long cavity limit. As a harmonically mode-locked laser is a phase-invariant system, each pulse possesses its own phase and position within the cavity round-trip. As such, a minimal model for the dynamics should be characterized by two degrees of freedom for each pulse: position and phase. Note that these quantities are not necessarily independent as the pulses have several possibilities to interact with each other via carrier dynamics and/or their coherent overlapping due to optical feedback or tail interactions. Since both mechanisms are inherently asymmetric, the resulting interactions are in general non-reciprocal [21]. First, we focus our analysis on the simplest case of two pulses circulating the cavity in the regime of temporal localized states. Starting with an established Haus

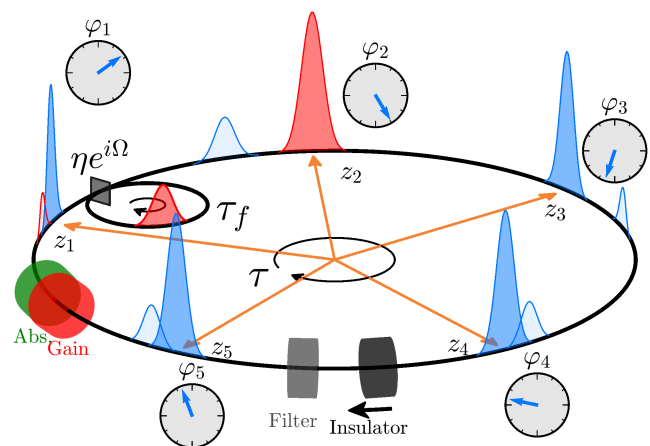


Figure 1: Schematic of a unidirectional ring cavity of length τ . The cavity is mode-locked by a saturable absorber and coupled to a time-delayed feedback loop with round-trip time τ_f , feedback rate η and phase Ω . Each pulse circulating possesses a phase φ_i and position z_i . The pulses are non-equidistant and their respective satellites induced by time-delayed feedback exhibit different amount of overlap with neighboring pulses.

*Corresponding author

✉ gurevics@uni-muenster.de (S.V. Gurevich)

ORCID(s):

master equation model, we derive a set of EOM for the positions and phases of the pulses. Our effective theory allows us to disclose highly complex dynamics that would be hardly accessible by other means. In particular, we demonstrate the existence of regimes in which pulses can be equidistant or non-equidistant and also have different phase relations. Multistability between regimes is also observed as well as emerging limit cycles and global heteroclinic bifurcations. From the intuition gained by studying the regimes with two pulses we infer the dynamics observed in the many pulses regimes where clustering, oscillations and chaos can readily be observed. Finally, we compare the results of the EOM with those of the full HME model showing excellent quantitative agreement.

Mode-locking can be experimentally implemented using mirrors to connect the various optical elements and to control the beam shape and the cavity stability. Alternatively, lenses may perform similar functions. However, even with high-quality lenses using anti-reflection coating, minute amounts of optical feedback occur thereby leading to time-delayed feedback perturbations. Notice that time-delayed feedback can also be applied on purpose to control the rich nonlinear passive ML dynamics, e.g., improving the time jitter in high repetition rate mode-locked lasers, controlling the pulse train repetition rate or acting as a solution selector that either reinforces or hinders the appearance of one of the multistable harmonic ML solutions [22, 23, 24, 25, 26, 27, 28]. The presence of time-delayed feedback in a mode-locked laser creates a non-local coupling between pulses [29] resulting in smaller copies, or satellites, of the main pulses to appear throughout the cavity. Depending on the satellites position they can lead to instabilities of the harmonic mode-locked state [27, 28] and enable the exchange of phase information between pulses over distances much larger than their typical pulse width. In particular, this can lead to a situation where the phase and position dynamics occurs on the same time scale such that neither of them are enslaved.

A sketch of the system in question is presented in Fig. 1. Here, we consider a passively mode-locked unidirectional ring laser with round-trip time τ that contains a gain section and a saturable absorber that enables pulsed emission. Further, a linear bandpass filter ensures that only certain laser modes are amplified, while others are suppressed whereas an optical isolator ensures unidirectional propagation. Additional couplings arising from time-delayed feedback [27, 28], or intra-cavity lenses reflection are modeled by an external time-delayed feedback loop of the length τ_f , the feedback rate η , and the feedback phase Ω . As was mentioned above, time-delayed feedback creates a small satellite for each pulse, which position depends on the ratio τ/τ_f , e.g. the red colored pulse in Fig. 1 creates the red satellite. Note that the pulses shown in Fig. 1 are not equidistant such that the overlap between pulses and satellites differs.

The interaction of pulses in mode-locked lasers was investigated in detail in the last decades using both experimental, theoretical and numerical tools in e.g., fiber laser

cavities [30, 31, 32, 33], solid-state laser with slow saturable absorber [34], figure-of-eight mode-locked fiber laser [35], optical loop mirror–nonlinear amplifying loop mirror mode-locked laser [36], passively mode-locked vertical-cavity surface-emitting lasers [15] or an array of nearest-neighbor coupled passively mode-locked lasers [37]. Recently, weak interactions of well-separated temporal localized states in semiconductor laser mode-locked by a saturable absorber and operated in the long cavity regime was studied analytically and numerically using a delay differential equations model [38]. With the aid of the EOM for the position- and phase-differences it was demonstrated that different configurations are obtained by a balance of gain and absorber interactions which depend on the linewidth-enhancement factors. In particular, it was discussed that the pulse interaction can be separated into incoherent long-range interaction mediated by carriers dynamics and coherent short-range interaction via pulse overlapping tails [36, 38]. Here, we focus on the influence of the coherent long-range interaction enabled by the presence of time-delayed feedback. We employ the Haus master equation (HME) [1] to model the optical field in the longitudinal direction while assuming a constant transversal mode. The HME can be derived from the time-delayed description in [39] using the assumptions of small gain, losses, and weak spectral filtering [40]. This leads to the coupled evolution of the electric field (E), the gain (g) and absorber population (q),

$$\partial_\xi E = \left(\frac{1}{2\gamma^2} \partial_z^2 + \frac{1 - i\alpha_g}{2} g - \frac{1 - i\alpha_q}{2} q - k \right) E + \eta e^{i\Omega} E(z - \tau_f), \quad (1)$$

$$\partial_z g = \Gamma (g_0 - g) - g |E|^2, \quad (2)$$

$$\partial_z q = q_0 - q - sq |E|^2. \quad (3)$$

Here, z and ξ denote the fast and slow time scales which describe the evolution within one round-trip and from one round-trip to the next one, respectively. Time is normalized to the absorber recovery time, g_0 is the pumping rate, Γ is the gain recovery rate, q_0 is the value of the unsaturated losses that determines the modulation depth of the saturable absorber. Further, the gain bandwidth is γ , the cavity losses are k and $\alpha_{g,q}$ correspond to the line-width enhancement factors for semiconductor material, while the ratio of the saturation energy of the gain and the absorber media is s . Note that the HME (1)-(3) was originally derived for gain media that are slowly evolving on the time scale of the cavity round-trip, resulting in a quasi-uniform gain temporal profile within the cavity. However, recent generalizations of the HME [41, 42, 43] preserve carrier memory from one round-trip toward the next, allowing for the correct description of complex pulse trains such as harmonic ML regimes. Since we operate in the long cavity regime without the loss of generality we apply periodic boundary conditions. The phase and translational invariance of the electromagnetic field in the passively mode-locked laser operated in the long cavity regime allow each pulse $j \in [1, N]$ to possess

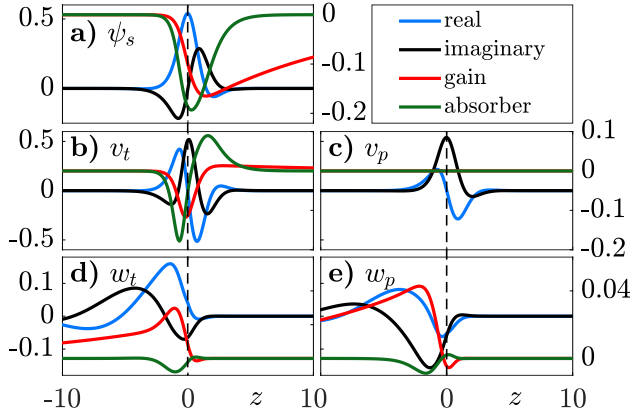


Figure 2: Exemplary stationary profiles of the (a) field and carrier components ψ_s , (b) translation and (c) phase neutral eigenfunctions and (d) translational (e) phase neutral eigenfunctions of the adjoint eigenvalue problem. For all panels, the left and right axis stands for the field and the carrier components, respectively. Parameters are $(\gamma, k, \alpha_g, \alpha_q, g_0, \Gamma, q_0, s) = (5, 0.1056, 1.5, 0.5, 0.99g_{\text{th}}, 0.08, 0.268, 10)$ in a domain of length $\tau = 200$. We use a discretization of 2048 points.

different phases φ_j and positions z_j , see Fig. 1 for $N = 5$. The lasing threshold g_{th} is determined by the pump level g_0 for which the off solution $(E, g, q) = (0, g_0, q_0)$ becomes linearly unstable and is defined by $g_{\text{th}} = q_0 + 2k$. Since we operate in the regime of temporal localized states, we choose $g_0 < g_{\text{th}}$. We note that in our formalism weak time-delayed feedback appears as a non-local spatial term with amplitude η and phase Ω in the field equation.

One can readily solve the HME (1)-(3) numerically in the long cavity regime with periodic boundary conditions using, e.g., the pseudo-spectral split-step semi-implicit scheme presented in Appendix B while ensuring to use a fine enough mesh in order to prevent effects imposed by the discretization [44]. From that, one can extract the dynamical information for the position and the phases of the resulting pulses. However, both the phases and the positions of the pulses evolve on a slow timescale which would require long time simulations over 10^5 of round-trips. Hence, in order to access the effective information of φ_j and z_j and the pulse interactions, we derive the *effective equations of motion*. The EOM provide a general interaction law between N pulses in the cavity and is achieved by projecting the high-dimensional dynamics of the HME (1)-(3) onto the low-dimensional subspace of the slowly evolving phase and translation modes. We rewrite the HME (1)-(3) for a real-valued vector function $\psi = (\text{Re}(E), \text{Im}(E), g - g_0, q - q_0)^T$ yielding

$$M \partial_{\xi} \psi = \mathcal{L} \psi + \mathcal{N}(\psi) + \eta e^{i\Omega} M \psi(z - \tau_f), \quad (4)$$

where $M = \text{diag}(1, 1, 0, 0)$ is a mass matrix and \mathcal{L} and \mathcal{N} are linear and nonlinear operators, respectively. Defining

$$\psi_s = \psi_{s,f} + \psi_{s,c} = (\text{Re}(E_s), \text{Im}(E_s), g_s - g_0, q_s - q_0)^T$$

as a stationary solution of Eq. (4), which is composed of the stationary solution for the field components $\psi_{s,f} =$

$(\text{Re}(E_s), \text{Im}(E_s), 0, 0)$ and the carrier components $\psi_{s,c} = (0, 0, g_s - g_0, q_s - q_0)$, we can employ the ansatz that a multi-pulse state Ψ is the sum of multiple stationary pulses ψ_s which are shifted and rotated with respect to each other. We denote the shifts z_j and rotations φ_j , respectively (cf. blue and orange arrows in Fig. 1):

$$\Psi = \sum_{j=1}^N \psi_j + \delta\psi, \quad (5)$$

where $\delta\psi$ accounts for small deviations from the simple summation and

$$\psi_j = R(\varphi_j) \psi_s(z - z_j(\xi)), \quad (6)$$

where $R(\varphi)$ is a matrix that rotates the field components of ψ_s by a phase φ . The four profiles of the vector function ψ_s calculated for a typical parameter set are shown in Fig. 2 (a). Plugging the ansatz (5) into Eq. (4) and linearizing around the stationary solution ψ_s leads to the linear eigenvalue problem $\mathcal{J}_s v = M \lambda v$ where \mathcal{J}_s is the Jacobian. The latter possesses two neutral eigenvalues corresponding to two neutral eigenfunctions $v_t = \partial_z \psi_s$ and $v_p = \partial_{\varphi} \psi_s$ for the translational and phase invariance, respectively, see Fig. 2 (b), (c). In the next step, we calculate the eigenmodes w_t and w_p of the corresponding adjoint linear system defined by $\mathcal{J}_s^{\dagger} w = M \bar{\lambda} w$, see Fig. 2 (d), (e) for the corresponding profiles.

The core of the EOM derivation consists in noticing that the perturbation $\delta\psi$ in Eq. (5) must remain small and bounded. As such, all the terms in the EOM must be orthogonal to the kernel of \mathcal{J}_s since, otherwise, $\delta\psi$ would grow without bound. This condition is achieved by projecting onto the adjoint eigenmodes w_t and w_p and using that (v_i, w_i) form a biorthogonal set. We further assume that the pulses are well-separated so that the interactions are weak, and that we can neglect shape deformation modes. Finally, note that we are considering the solution basis for the case of zero feedback. This approach allows us to add weak feedback as a source of motion and phase dynamics. In other words, the time-delayed feedback induced satellites are treated as a first order perturbation. In practice, it means that the feedback induced satellites are small enough that they do not induce any interaction with the carriers. This leads to the following EOM (see Appendix A for the complete derivation):

$$\begin{aligned} \partial_{\xi} \varphi_m &= \sum_{k \neq m} [B_p(\Delta_{km}) + \eta L_p(\tau_f + \Delta_{km}) \times \\ &\quad \sin(\Omega + \theta_{km} + u_p(\tau_f + \Delta_{km}))], \\ \partial_{\xi} z_m &= \sum_{k \neq m} [B_t(\Delta_{km}) + \eta L_t(\tau_f + \Delta_{km}) \times \\ &\quad \sin(\Omega + \theta_{km} + u_t(\tau_f + \Delta_{km}))]. \end{aligned} \quad (7)$$

Here, we define the phase and position differences $\theta_{km} \equiv \varphi_k - \varphi_m$ and $\Delta_{km} \equiv z_k - z_m$. Further, $B_{t,p}(\Delta_{km})$, $L_{t,p}(\Delta_{km})$ and $u_{t,p}(\Delta_{km})$ are nonlinear functions, giving the information about the interaction strength. These forces result

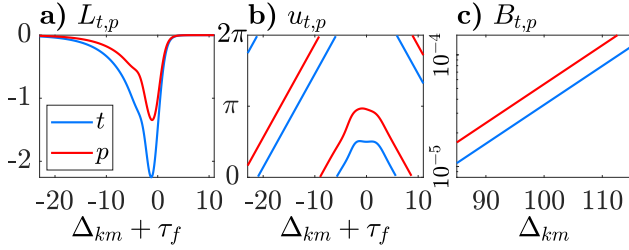


Figure 3: Numerically computed nonlinear force contributions $L_{t,p}$, $u_{t,p}$ and $B_{t,p}$ of EOM (7), (8) as a function of Δ_{km} . All the forces are periodic functions with a periodicity of τ . Note, that panel (c) is given on a logarithmic scale. Parameters are as in Fig. 2. Formal definitions given in App. A, Eqs. (A.24), (A.25) and (A.27), respectively.

from overlap integrals between the adjoint eigenvectors and the solution profile (see App. A, Eqs. (A.24), (A.25), (A.27) for the formal definition) and their numerically computed profiles are depicted in Fig. 3. We note, that we neglect the phase-dependent force stemming from the overlapping tails (cf. term with coefficient $A_{t,p}$ in Eqs. (A.30,A.31)). Assuming exponential tails, this interaction scales as $\exp(-\Delta_{km}/\tau_p)$ where τ_p is the pulse width. With $\tau_p \approx 2$ (cf. Fig. 2(a)) and $\Delta_{km} \approx 100$, this force is extremely weak compared to the other relevant forces (cf. Fig. 3). That is, the relevant forces stem from gain repulsion and interaction via time-delayed feedback, respectively.

While Eqs. (7),(8) consider interactions between all pulses, generally nearest neighbor interactions provide the leading order term. Note that the efficiency of the EOM is that the overlap integrals only need to be evaluated once for a particular set of system parameters. They can then be applied independently of the pulse number and the feedback parameters η , Ω and τ_f .

Analyzing the general structure of the EOM (7),(8) one notices that both the position and phase terms are composed of two parts: a phase-independent term $B_{t,p}$ (cf. Fig. 3 (c)) stemming from interaction between pulses via carriers (which only depend on the intensity) and the presence of non-zero linewidth enhancement factors, and a phase-dependent term stemming from the interaction via time-delayed feedback. In fact, the phase-independent force $B_{t,p}$ can be calculated analytically. It is defined as (cf. App. A)

$$B_{t,p}(\Delta) = \frac{1}{N_{t,p}} \langle w_{t,p} | \mathcal{J}_s \psi_{s,c}(z - \Delta) \rangle, \quad (9)$$

where $N_{t,p}$ are the normalization factors for the translation and phase part, respectively, which read

$$N_p = \langle w_p | M v_p \rangle, \quad N_t = -\langle w_t | M v_t \rangle,$$

and $\langle \cdot | \cdot \rangle$ is a scalar product. First, as the gain recovers much slower than the absorber ($\Gamma \ll 1$), we can neglect the attracting effect of the saturable absorber such that the phase-independent force is governed by gain repulsion [38]. We define z_0 as the position, where the pulse has decayed

sufficiently such that one can assume exponential recovery. Hence, we obtain

$$\psi_{s,g}(z) = T \begin{cases} e^{-\Gamma z} & z > z_0 \\ e^{-\Gamma(z+\tau)} & z < z_0 \end{cases}, \quad (10)$$

where $T = [g(z_0) - g_0] e^{\Gamma z_0}$. The factor of $e^{-\Gamma \tau}$ in the second equation has to be added due to the periodicity of the domain. From Eq. (10) one can see that $\psi_{s,g}(z - \Delta) = e^{\Gamma \Delta} \psi_{s,g}(z)$ which can be used to solve the scalar product in Eq. 9. One obtains

$$B_{t,p}(\Delta) = C_{t,p} e^{\Gamma \Delta}, \quad (11)$$

$$\text{where } C_{t,p} = \frac{T}{N_{t,p}} \langle w_{t,p} | \mathcal{J}_s (e^{-\Gamma(z+\tau)} e_g) \rangle.$$

Here, e_g is a unit vector with components in the gain part. For more details, see App. A.7. Hence, we see that as the carrier recovers exponentially, the phase-independent force is an exponential as well. We note that the attracting interaction via the absorber also follows an exponential and can be derived in the same way [38]. The interaction scales as $\exp(-1 \cdot \Delta_{km})$, where the coefficient of 1 stems from the normalization of Eqs. (1-3) with respect to the absorber recovery rate. For separations of $\Delta_{km} \approx 100$ which we consider in the following, the interaction is $\sim 10^{-44}$ which safely can be neglected compared to the gain interaction which is $\sim 10^{-4}$. While the exponential interaction in eq. (11) can be understood intuitively for the dynamics of the pulses' positions z_j , it can be surprising that the phases φ_j are also influenced by a phase-independent force. The answer to this lies in the line-width enhancement factors $\alpha_{g,q}$ which couple the real and imaginary parts of the electric field, i.e. for $\alpha_{g,q} = 0$ we find $B_p(\Delta) = 0$.

In order to visualize the derived EOM (7), (8), we start with a simple configuration where two pulses with the positions $z_{1,2}$ and phases $\varphi_{1,2}$ circulate in the cavity, leading to a two-dimensional phase space spanned with one position and one phase difference $\Delta_{21} = \Delta = z_2 - z_1$ and $\theta_{21} = \theta = \varphi_2 - \varphi_1$, respectively. Here, the flow is described by the two ODEs $\dot{\Delta}(\Delta, \theta)$ and $\dot{\theta}(\Delta, \theta)$ which follow directly from the EOM (7), (8) (cf. App. A.6.3, Eqs. (A.38), (A.39)). First, it is instructive to look at symmetries in the resulting equations. From Eqs. (7),(8) we can directly see, that $\dot{\Delta}(\Delta, \theta) = -\dot{\Delta}(-\Delta, -\theta)$ (the same property holds for $\dot{\theta}$). This property can be concluded from the exchanging the numbering of the two pulses. Further, $\dot{\Delta}$ and $\dot{\theta}$ are τ - and 2π -periodic in the first and second variable, respectively. Therefore, one obtains

$$\dot{\Delta}(\Delta, \theta) = -\dot{\Delta}(\tau - \Delta, 2\pi - \theta).$$

Having that in mind, we can directly deduce two steady states: $(\Delta^*, \theta^*) = \left(\frac{\tau}{2}, \pi\right)$ and $(\Delta^*, \theta^*) = \left(\frac{\tau}{2}, 0\right)$. That is, at $\Delta = \frac{\tau}{2} \pm \delta$, $\theta = \pi \pm \alpha$ one obtains

$$\dot{\Delta}\left(\frac{\tau}{2} + \delta, \pi + \alpha\right) = -\dot{\Delta}\left(\frac{\tau}{2} - \delta, \pi - \alpha\right). \quad (12)$$

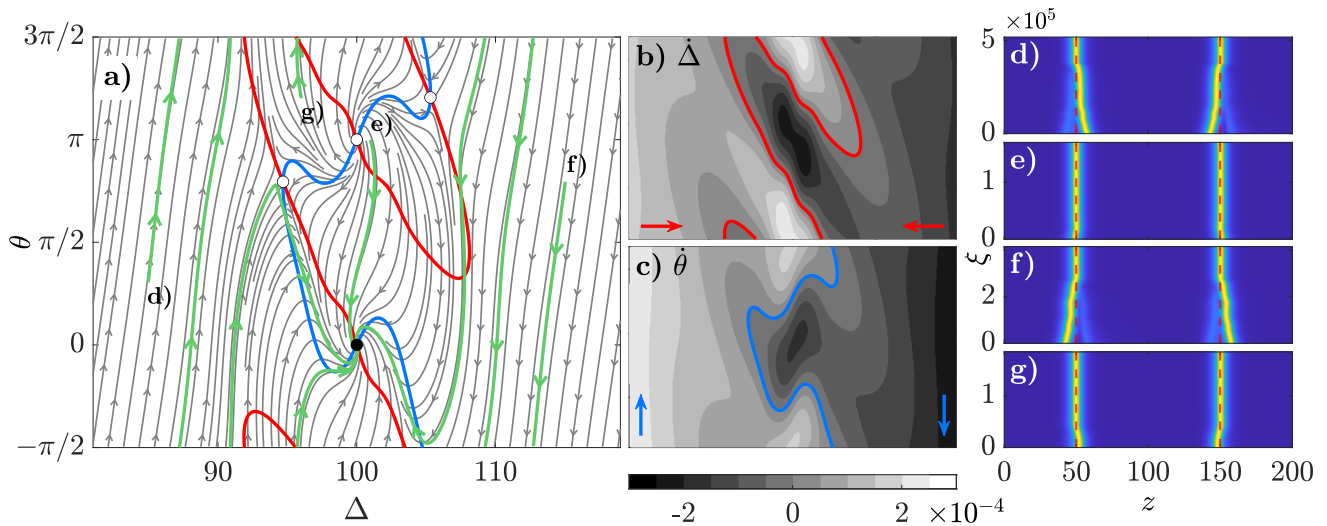


Figure 4: (a) Vector field diagram of the phase space (Δ, θ) governed by the EOM (7),(8) for two pulses. Red and blue contour lines correspond to the Δ - and θ -nullclines, respectively. Black (white) circles at the intersections of the nullclines correspond to stable (unstable) fixed points. Light green lines correspond to four exemplary trajectories obtained from time simulations of the full HME (1)-(3). The respective two-time representations of the intensities are shown in (d)-(g). There, vertical red dashes lines indicate the equidistant position, i.e., $z_1 = 50, z_2 = 150$. (b),(c) The magnitude of $\dot{\Delta}$ and $\dot{\theta}$, respectively. (d)-(g): Four exemplary time traces corresponding to the four initial states in (a). To emphasize the presence of the satellite, the colormap corresponds to $|E|^{1/4}$. Parameters are: $\tau_f = 100, \eta = 10^{-4}, \Omega = \pi/4$, other parameters as in Fig. 2.

Next, for the sake of simplicity, we start with the case of resonant feedback, i.e., the situation when the pulse satellite of a pulse induced by the feedback loop coincides with another pulse, i.e., $\tau_f = \tau/2$ for $\tau = 200$. The other parameters are set to $\Omega = 0.25\pi$ and $\eta = 10^{-4}$ such that the interactions via time-delayed feedback and carriers are in the same order of magnitude (cf. y -scales in Fig. 3). For each point in the phase space (Δ, θ) , one can evaluate the flux of the EOM (7),(8) and reconstruct the corresponding vector field, see Fig. 4 (a). Due to the aforementioned symmetries, we find the one stable $(\Delta^*, \theta^*) = (\tau/2, 0)$ (filled circle) and one unstable $(\Delta^*, \theta^*) = (\tau/2, \pi)$ (open circle) fixed point, corresponding to the equidistant configurations. Furthermore, we find two other steady states corresponding to non-equidistant configurations. In Fig. 4 (a) they are placed at around $\Delta \approx 95$ and $\Delta \approx 105$, however, they are both unstable.

At this point, we want to emphasize the excellent quantitative predictions by the EOM. For that, we performed four DNSs (cf. black labels (d)-(g) in Fig. 4 (a) for the corresponding initial conditions) of the full HME (1)-(3) with two pulses, see also Fig.4 (d)-(g) for the two-time representation of the corresponding time traces. Here, vertical red lines visualize the equilibrium positions at $z_1 = 50$ and $z_2 = 150$ for $\tau = 200$ and $\tau_f = 100$. Note that in panels (d), (f) the effect of the satellites due to time-delayed feedback is especially visible: at the steady state, the one pulse is sitting on the satellite of the second one and vice versa.

From the resulting time trace, the positions and phases of the pulses are extracted and plotted as trajectories in the phase space (cf. green lines in Fig. 4 (a)). One can see that

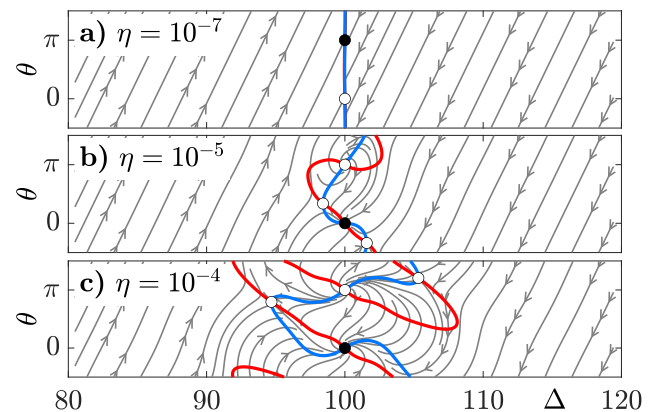


Figure 5: Vector field diagrams of the phase space (Δ, θ) governed by the EOM (7), (8) for two pulses for three different values of η . Red and blue contour lines correspond to the Δ - and θ -nullclines, respectively. Black (white) circles at the intersections of the nullclines correspond to stable (unstable) fixed points. Other parameters as in Fig. 4.

not only stable steady states are predicted correctly, but in the whole phase space the trajectories are tangent to the predicted vector field. Note that as the present interaction forces are small, the simulations of the HME (1)-(3) need to be performed over several 10^5 round-trips. This reveals a strong advantage of the EOM (7), (8) as the vector field for the complete phase space can be reconstructed in seconds versus hours it would take to achieve a similar result with the full HME model.

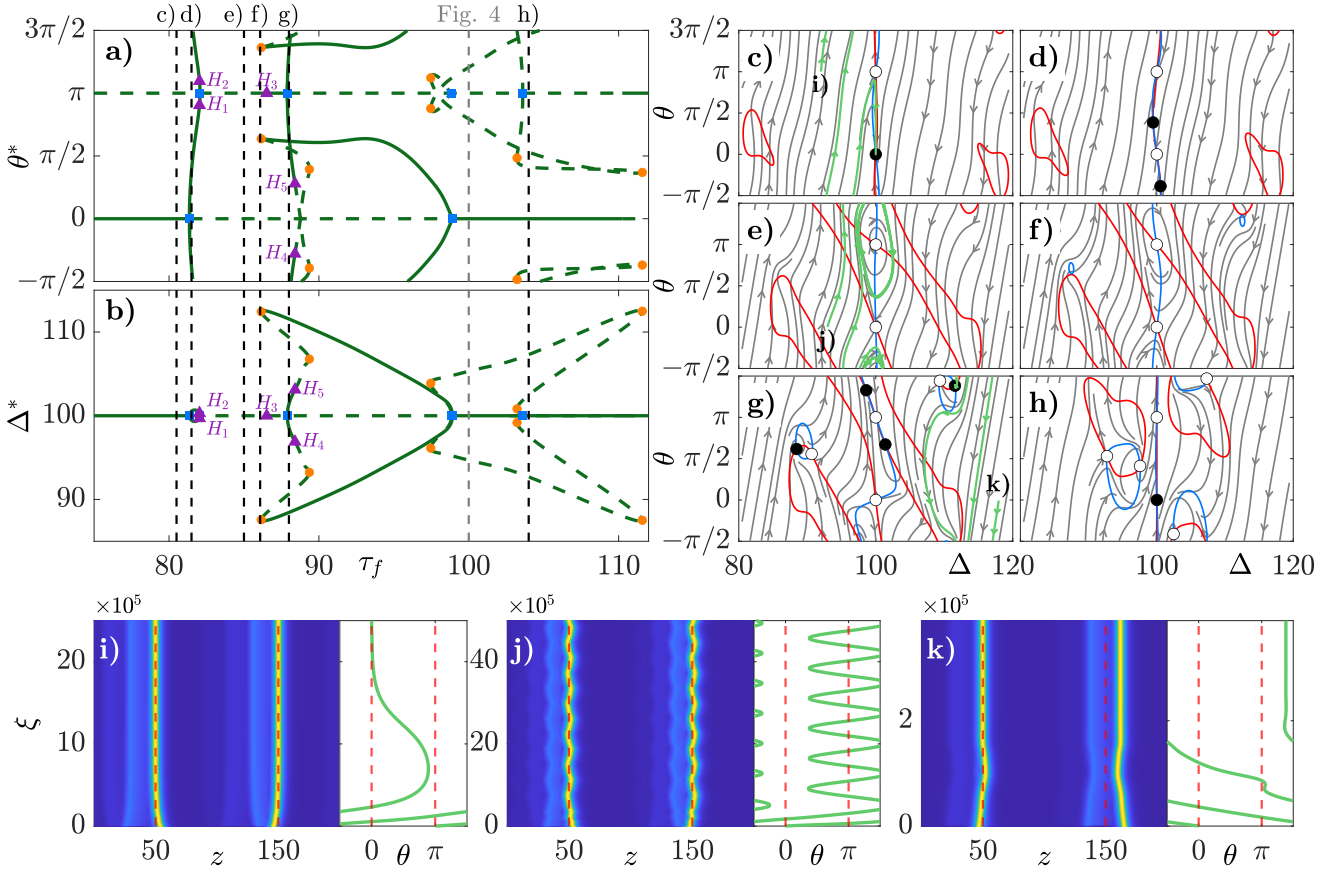


Figure 6: (a),(b) Bifurcation diagrams in τ_f of the EOM (7),(8) for $\eta = 10^{-4}$ and $\Omega = \pi/4$ showing steady states (θ^* , Δ^*) in phase and position differences, respectively. Solid (dashed) green lines stand for stable (unstable) unstable solutions. Purple triangles, blue squares and orange dots correspond to AH, pitchfork and saddle-node bifurcation points, respectively. (c)-(h) Vector field diagrams for values of τ_f indicated by black dashed lines in panels (a) and (b). Red and blue contour lines correspond to the Δ - and θ -nullclines, respectively. Black (white) circles at the intersections of the nullclines correspond to stable (unstable) fixed points. See the supplemental material for a scan through the bifurcation diagram. (i)-(k) Result of time simulations of the full HME (1)-(3) where equidistant positions and phases are indicated by red dashed lines. The corresponding trajectories are shown in panels (c), (e) and (g), respectively. Other parameters as before.

In this case the feedback delay $\tau_f = 100$ was chosen such that it mainly acts around the equidistant position at $\Delta = 100$. The width of the area where the feedback has a strong influence is given by the width of the amplitude of the phase-dependent force $L_{t,p}$ (cf. Fig. 3 (a)). In regions, where the influence of the feedback is small ($\Delta \lesssim 90$ and $\Delta \gtrsim 110$), the system is driven by gain repulsion. This force pushes the pulses to equidistance, hence, it points towards the center (cf. red arrows in Fig. 4 (b)), where the magnitude of Δ is shown together with its nullcline (red contour line). At the same time, due to the carrier frequency, the phase changes at a similar rate (cf. blue arrows and θ nullcline in Fig. 4 (c)), resulting in the effective diagonal motion in the phase space (cf. Fig. 4 (a)).

For the results presented in Fig. 4, the value of η was chosen in a way that the phase-dependent force is in the same order of magnitude as the phase-independent force. A situation, when this is not the case can be seen in Fig. 5, where the phase space (Δ, θ) together with the corresponding nullclines is presented for three values of η . One can see

in Fig. 5 (a), that for smaller values of η , the phase space is solely dominated by the force due to gain repulsion, which results in diagonal vector field lines towards the equidistant positions as discussed above. For larger values of η , more complex dynamics can appear as seen in Fig. 5 (b), (c). Note there is an upper bound for what values of η provide good predictions as in the derivation of the EOM (7),(8), it is assumed, that the satellite stemming from the time-delayed feedback loop does are not sufficiently intense to create a carrier depletion. While this is true for small values of η , this is not the case for large η .

In order to gain a full overview of the phase and position dynamics in dependence of the feedback parameters τ_f and Ω , we perform a detailed bifurcation analysis of the EOM (7),(8). It is conducted by calculating the vector field as was presented in Fig. 4, extracting the steady states (Δ^* , θ^*) from it and calculating its behavior by changing the control parameters.

The results of a scan in feedback delay time τ_f are presented in Fig. 6 (a),(b), where the equilibrium phase θ^*

and position Δ^* differences are shown, respectively. Note that the stable (solid line) and unstable (dashed line) steady states at $\theta^* = (0, \pi)$ in the panel (a) lie on top of each other in the panel (b) as they both correspond to the equidistant case $\Delta^* = 100$. Further, different phase space configurations, corresponding to different τ_f values labeled with the vertical black dashed lines in Fig. 6 (a),(b) are shown in Fig. 6 (c)-(h). Furthermore, the gray dashed line indicates the $\tau_f = 100$ -cut previously presented in Fig. 4 (a).

One can see that the bifurcation diagrams in Fig. 6 (a),(b) reveal a complex dynamics with many interesting regimes. First, at low values of τ_f , there are only the two fixed points corresponding to the in-phase and anti-phase equidistant configurations (cf. filled and open circles in Fig. 6 (c)), where both Δ (red) and θ (blue) nullclines cross). This means that the satellites are too far away from the pulses for them to interact. This is emphasized by the green trajectory corresponding to the result of a time simulation where the pulses settle on an equidistant configuration (cf. also Fig. 6 (i)). However, in the final state pulses and satellites exhibit small overlap which is in contrast to the situation shown in Fig. 4 (d)-(g). This results in a de facto decoupling of phase and position dynamics as the pulses quickly settle on an equidistant state, yet the phases take much longer to reach the steady state.

Next, by increasing τ_f , two non-equidistant configurations emerge from the in-phase solution $\theta^* = 0$ (cf. Fig. 6 (d)) in a pitchfork bifurcation (cf. blue square in Fig. 6 (a)). Further, on these branches, two Andronov-Hopf (AH) bifurcations denoted H_1 and H_2 occur leading to the emergence of time-periodic solutions. In fact, in the range of $\tau_f \approx [82, 86]$, all fixed points are unstable such that the limit cycle is the only stable manifold. This can be seen in the phase-space in Fig. 6 (e). Here, the green line is a trajectory obtained from a time simulation of the full HME (1)-(3) which confirms the presence of a stable periodic orbit. The two-time representation of the trace is shown in Fig. 6 (j). Again, the quantitative agreement between the HME and the EOM is excellent.

To clarify the question, why only one stable limit circle emerges in time-simulations, we consider the three-dimensional space $(\Delta^*, \theta^*, \tau_f)$ in an interval $\tau_f \approx [80, 88]$, see Fig. 7. A detailed bifurcation analysis reveals that the AH bifurcations $H_{1,2}$ are subcritical and the two unstable periodic orbits connect in a double-homoclinic bifurcation leading to a single unstable limit cycle. The latter undergoes a saddle-node bifurcation resulting in a single stable limit cycle (cf. inset in Fig. 7). Note that the emerging periodic orbit oscillates around the equidistant steady state $(\Delta^*, \theta^*) = (100, \pi)$. Further, the periodic branch merge with the equidistant steady state branch again in the subcritical AH bifurcation H_3 around $\tau_f \approx 86$. Furthermore, around $\tau_f \approx 88.5$, we find another regime of periodic orbits. Here, they bifurcate at points $H_{4,5}$ from two branches emerging from a pitchfork bifurcation of the equidistant steady state (cf. Fig. 7). However, the AH bifurcations H_4 and H_5 are supercritical, i.e. one finds stable periodic orbit oscillating

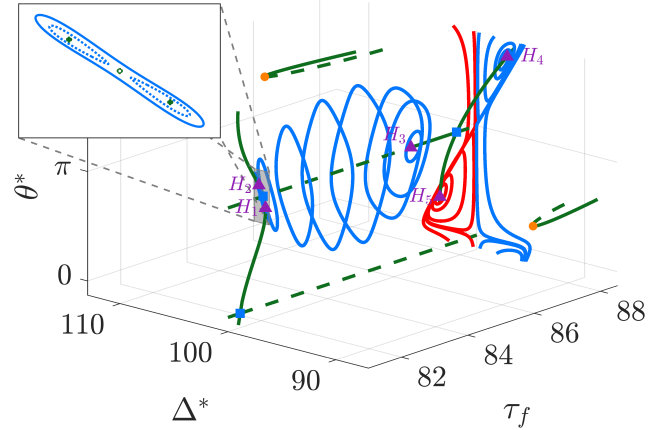


Figure 7: Three-dimensional phase space spanned by $(\tau_f, \Delta^*, \theta^*)$ of the EOM (7),(8). Steady states are depicted in green and emerging periodic solutions in blue and red. Purple triangles, blue squares and orange dots correspond to AH, pitchfork and saddle-node bifurcation points, respectively. The inset shows a single stable limit cycle, resulted from a double-homoclinic bifurcation followed by a saddle-node bifurcation. For a two dimensional projection, see Fig. 6 (a),(b).

around the non-equidistant steady states. However, with increasing τ_f , these limit cycles from both sides recombine at the unstable equidistant steady states in homoclinic bifurcations such that the periodic orbits now perform full phase rotations of 2π .

Bringing our attention back to Fig. 6 after the regime of periodic solutions, we find a broad range of stable non-equidistant configurations. Figure 6 (f) indicates the presence of two saddle-node bifurcations (cf. orange circles in Fig. 6 (a),(b) and Fig. 7), leading to the emergence of fixed point pairs. This corresponds to situations where one pulse sits on the satellite of the other pulse acting as an anchor, while its satellite does not interact with the other pulse, i.e. the coupling is unidirectional; cf. the time simulation in Fig. 6 (k). As the anchor satellite moves linearly with τ_f we can see an approximately linear response of the steady state position Δ^* in this regime. A particularly interesting situation can be seen in Fig. 6 (g), where four stable non-equidistant solutions coexist. The regime of stable non-equidistant states disappears in a pitchfork bifurcation (cf. blue square in Fig. 6 (a),(b) around $\tau_f \approx 100$) as the difference between the equidistant state and the time-delay τ_f approaches the pulse width. Then the satellite is absorbed into the main pulse which can be seen in form of a pitchfork bifurcation.

Finally, considering time delays larger than $\tau/2$, we do not observe other stable steady states than the equidistant ones, see Fig. 6 (h). This is because the interaction of the pulses with satellites is much stronger on the leading than on the trailing edge. As a result, the pulses are almost decoupled in this regime and hence, the equidistant steady states are only weakly stable and unstable, respectively. The fact that the interaction via satellites is not symmetrical around the pulse can already be observed in the form of the amplitude

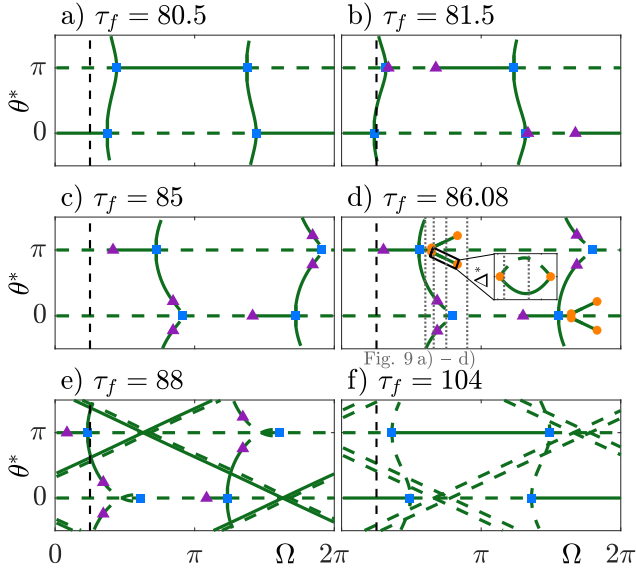


Figure 8: Bifurcation diagrams of the steady state θ^* as function of Ω for different values of τ_f (the same values as in Fig. 6 (c)-(h) are used). The black dashed line at $\Omega = \pi/4$ marks the cross-sections shown in Fig. 6 (c)-(h). In panel (d), the gray dashed lines correspond to the vector field diagrams presented in Fig. 9. The inset shows the appearance of the saddle-node bifurcation of steady states which lie inside the black rectangle on the position norm. See the supplemental material for scans through the shown bifurcation diagrams.

of force $L_{t,p}$ in Fig. 3 (a) which has a much larger tail on the leading side than on the trailing edge. This property is inherited from the asymmetric pulse profile shown in Fig. 2 (a).

Next, we consider the influence of the feedback phase Ω on possible pulse configurations. First, we notice a further symmetry in the EOM (7,8):

$$\dot{\Delta}(\Delta, \theta, \Omega) = \dot{\Delta}(\Delta, \theta + \pi, \Omega + \pi). \quad (13)$$

The same relation holds for $\dot{\theta}$. The symmetry can be observed in Fig. 8, where bifurcation diagrams in Ω for various values of τ_f are shown. In all panels the black vertical dashed lines correspond to the cuts at $\Omega = \pi/4$ corresponding to the phase spaces shown in Fig. 6 (c)-(h). In Fig. 8 (a), one can see that when pulse and satellite are far from each other, stable non-equidistant states resulting from the pitchfork bifurcations (cf. blue squares) can only occur for a very narrow range of the feedback phases as interactions are weak in this regime. Slightly increasing τ_f (cf. panel (b)) enables the emergence of AH bifurcations (see the purple triangles) leading to periodic solutions whose range in Ω increases for larger values of τ_f (cf. panel (c)). Next, increasing Ω , we find multistability of non-equidistant states as two pairs of saddle-node bifurcations (cf. orange circles panel (d)) emerge (cf. the inset).

To further understand this emergence, we consider the phase-space (Δ, θ) for four values of the feedback phase in Fig. 9. There, one can observe the nullclines of phase-

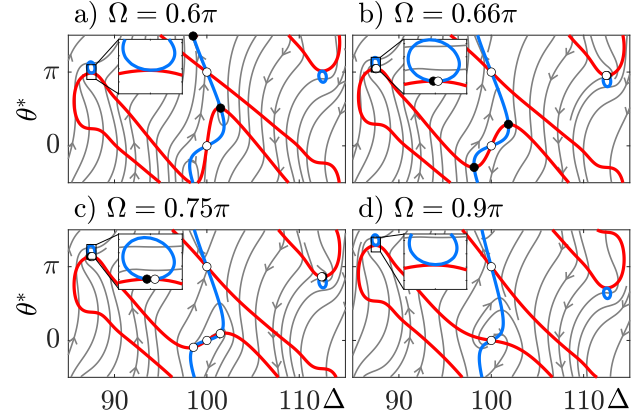


Figure 9: Vector field diagrams evaluated at positions marked in Fig. 8 (d) by gray dashed lines. Red and blue contour lines correspond to the Δ - and θ -nullclines, respectively. Black (white) circles at the intersections of the nullclines correspond to stable (unstable) fixed points. The insets show close-ups on the area at around $\Delta \approx 88$, where a pair of fixed points emerges (b,c) and vanishes (a,d) in a saddle-node bifurcation. Due to the symmetry around $\Delta = 100$, a pair of fixed points emerges simultaneously at around $\Delta \approx 112$.

and position-dynamics to be very close (cf. the inset in panel (a)). Next, in panels (b) and (c), they intersect which explains the emergent stable and unstable steady states (cf. the insets). This fixed points exists far away from equidistant states and corresponds to the situation where one pulse sits on satellite of the second pulse, while the satellite of the second pulse does not interact with the first pulse. Finally, the nullclines separate again (cf. panel (d)). Interestingly, in Fig. 8 (e) the aforementioned non-equidistant configuration exists for all Ω as becomes evident by the emerging cross-shaped structure of the trajectories. Further, this shape reveals that the pulse's phase relation in this case depends almost perfectly linearly on Ω . At the same time, it was shown in Fig. 6 (b), that in this regime the position also depends linearly on τ_f , i.e. in this case the time-delayed feedback parameters directly control the pulse configuration in phase and position. Finally, in Fig. 8 (f) for $\tau_f = 104$, all non-equidistant steady states became unstable and only – depending on Ω – the in-phase or anti-phase configurations remain stable, which, however, can be bistable for a small parameter range.

Finally, we summarize the findings in the two-parameter bifurcation diagram on the plane (τ_f, Ω) in Fig. 10. Here, the positions of all the previously shown one-parameter diagrams and corresponding phase spaces are marked by dashed lines and red crosses, respectively. Blue, orange and purple lines correspond to the pitchfork, saddle-node and AH lines. First, we notice the π -periodicity in Ω due to Eq. (13). Further, the colormap encodes the number of stable steady states. In white regions, where no steady state is stable, periodic solutions are the global attractors. Non-equidistant states always appear in pairs due to symmetry reasons. Hence, in regions with an odd number of stable

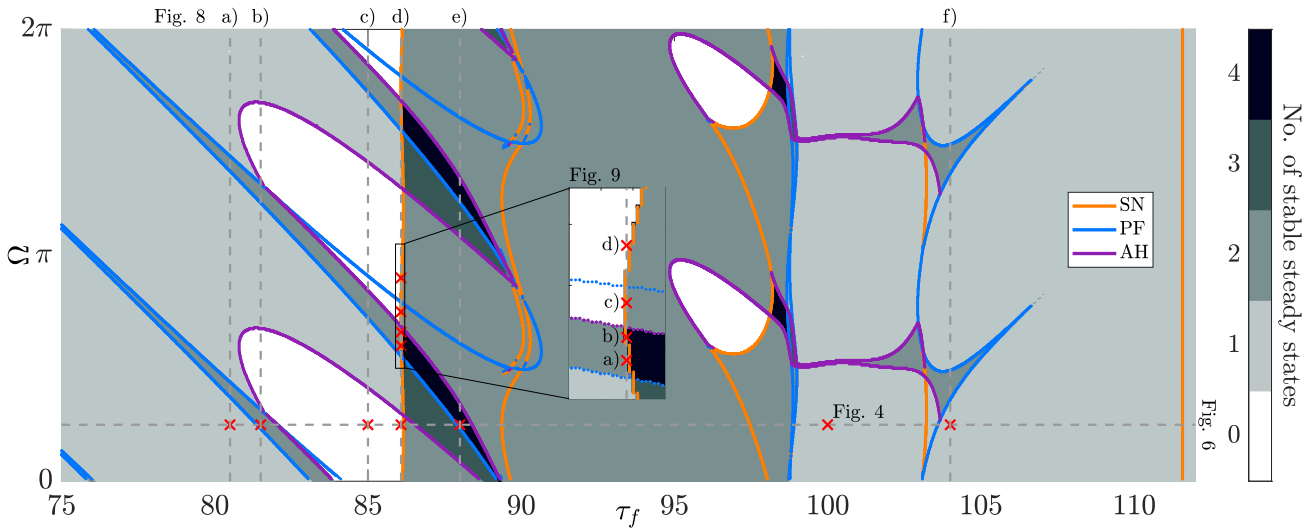


Figure 10: Two-parameter bifurcation diagram in the (τ_f, Ω) -plane. Orange, blue and purple lines stand for saddle-node (SN), pitchfork (PF) and AH bifurcations, respectively. The colormap encodes the number of stable steady states of EOM (7),(8). Dashed lines correspond to the cross-sections where one-parameter bifurcation diagrams are shown in Fig. 6 (a),(b) and Fig. 8. At the positions marked with red crosses the phase spaces are presented in Figs. 4, 6 (c)-(h) and Fig. 9.

steady states, one of the equidistant configurations must be stable. On the other hand, in regions with an even number of steady states, either both equidistant states are stable or only non-equidistant states are stable. While the aforementioned case only applies in a small range of parameter values where $\tau_f > 100$ (cf. Fig. 8 (f)), the latter regime dominates the range of $\tau_f \in [87, 97]$.

So far, we presented the results of a system consisting of two pulses, i.e. a two-dimensional phase space. However, the EOM (7,8) is valid for an arbitrary number of pulses. In fact, we can reuse the calculated profiles and eigenfunctions (cf. Fig. 2) and define them over a cavity of length $\tau_N = \frac{\tau}{2}N$ as they all decay to zero. Then, as the profiles and eigenmodes remain unchanged, the forces $L_{t,p}, u_{t,p}, B_{t,p}$ (cf. Fig. 3) remain the same as well but just need to be defined on a larger domain. However, $L_{t,p}$ converges to zero when its argument is not in the vicinity of zero (such that it is not necessary to compute $u_{t,p}$ on a larger domain) and $B_{t,p}$ is known analytically. This enables us to predict the system's behavior even though the phase space of higher dimensional systems cannot be visualized easily.

It was demonstrated that in the range where gain repulsion is dominant the two pulses converge exponentially to the equidistant configuration (cf. Fig. 5 (a)). This property can be generalized to N pulses neglecting the influence of feedback ($\eta = 0$). Here the gain repulsion is dominated by the first neighbor to the left, i.e. the EOM for the positions read

$$\dot{z}_n = B_t(z_{n-1} - z_n) \quad (14)$$

with the boundary conditions $z_0 = z_N - \tau$ and $z_{N+1} = z_1 + \tau$. Then the equidistant configuration is defined by $z_n^* = n\frac{\tau}{N} + v_0 t$ where v_0 is a constant drift. Using the ansatz $\delta_n = \sum_p a_p e^{\lambda_p \xi + i q_p n}$ for perturbations from these steady

states (where $q_p = \frac{2\pi}{N}p, p = 0, \dots, N-1$), one obtains (see App. A.6.4 for more details)

$$\lambda_p = B_t' \left(-\frac{\tau}{N} \right) [(\cos(q_p) - 1) - i \sin(q_p)] . \quad (15)$$

As $B_t' \left(-\frac{\tau}{N} \right) > 0$ (cf. Fig. 3 (c)) and $(\cos(q_p) - 1) < 0$, the steady state is stable as expected for all N . However, for $N \geq 3$ the imaginary part does not vanish such that these fixed points are stable spirals. To support this hypothesis we choose $N = 3$ as the complete position phase space can be visualized in the $(\Delta_{21}, \Delta_{32})$ -plane, see Fig. 11. Note that the complete phase space is four-dimensional. However, due to the absence of feedback the dynamics in the $(\theta_{21}, \theta_{32})$ -plane is decoupled from the dynamics in the $(\Delta_{21}, \Delta_{32})$ -plane.

Here, the green lines are obtained from three time simulations of the full HME model (1)-(3) and show excellent quantitative agreement with the flow predicted by the EOM (7),(8). Although the dynamics between pulses is given by a first order system of exponential relaxation, the ensemble give rise to oscillatory behavior and a oscillatory dynamics.

Finally, including the effects of time-delayed feedback and going to even higher harmonic numbers and taking the phase dynamics into account makes the resulting dynamics more and more complex due to the added degrees of freedom. Performing various time simulations of the EOM (7),(8) using different initial conditions and feedback parameters for $N = 6$ reveals a variety of possible configurations as presented in Fig. 12. Here, panels (a) and (b) show the resulting steady states difference $z_m - z_1$ for two different (τ_f, Ω) values, where the corresponding equidistant configurations are marked by dashed lines.

In particular, panel (a) shows a stable configuration, where the distance between neighboring pulses alternates

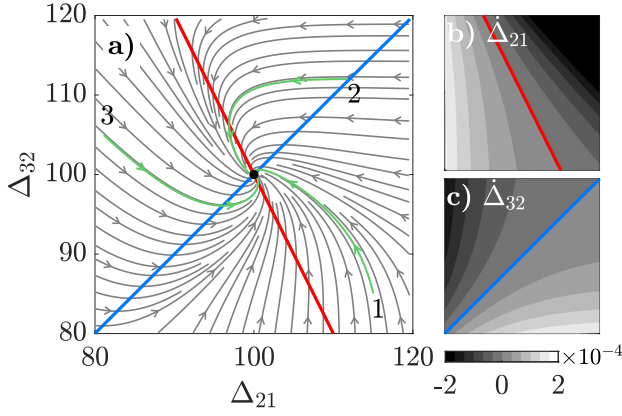


Figure 11: a) Vector field diagrams of the $(\Delta_{21}, \Delta_{32})$ -phase space for three pulses which dynamics is governed by the EOM (7), (8) for $\eta = 0$. Red and blue contour lines correspond to the Δ - and θ -nullclines, respectively. Black circle at the intersections of the nullclines correspond to the stable fixed point. The green lines are traces of three numerical simulations of the full HME (1)-(3) and show excellent quantitative agreement with the predictions of the EOM. The magnitude of $\hat{\Delta}_{21}$ and $\hat{\Delta}_{32}$ is plotted in panels (b) and (c), respectively.

between a higher and a lower value, i.e. there are three chunks of two bound pulses. This is analogous to the stable non-equidistant configurations found for two pulses (e.g. presented in Fig. 6 (d), (g), (k)). However, in panel (b), by a slight change in τ_f we find another solution, where two chunks of three bound pulses exist.

Further, panels (c)-(e) show various periodic states. In the panel (c), we see two position differences oscillating regularly, while the remaining exhibit a much smaller amplitude (cf. the insets). Figure 6 (d) presents a similar situation, however, the oscillations are not sine-like as before. Next, in panel (e), we find another periodic state which in this case has a much higher frequency, see the inset. Finally, also aperiodic oscillations can be found as shown in panel (f). Performing the simulations in panel (f) again with a small perturbation (10^{-10}) and comparing the two results, reveals that the trajectories diverge exponentially. To show this, we define σ as the Euclidian norm of the phase difference between the perturbed and unperturbed trajectories, i.e. their distance in phase space. The result is shown in the inset of Fig. 12 (f) where one can observe an exponential increase in σ . Hence, in this situation, the maximal Lyapunov exponent is positive and therefore, the system is chaotic.

In conclusion, we have demonstrated in this manuscript that the position and phase dynamics of a semiconductor ring laser in a multipulse configuration with N pulses can be described by effective equations of motion (EOM) defined by $2N$ ODEs. In particular, we studied the interaction between pulses under the influence of time-delayed feedback which results in satellites following the main pulses. This leads to strongly non-local interactions that manifest as long-range phase-dependent forces which compete with the phase-independent gain repulsion mediated by carrier

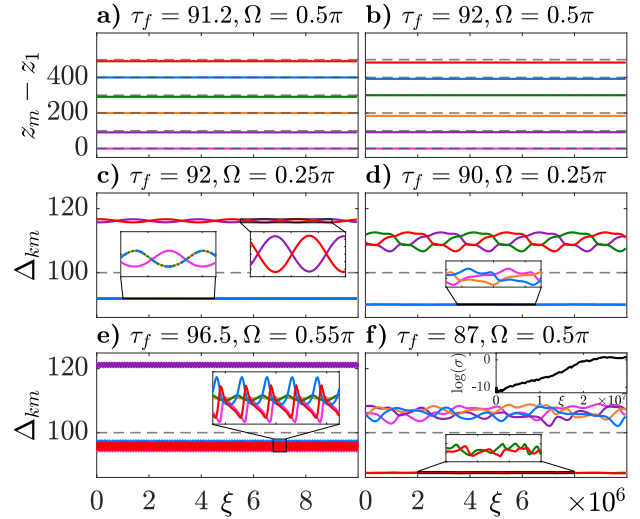


Figure 12: Time traces of numerical time simulations of EOM (7), (8) for six pulses for $\eta = 10^{-4}$ and for different values of τ_f and Ω yielding different configurations of phases and positions. (a) Two sets of three bound pulses. (b) Three sets of two bound pulses. (c)-(e) Different periodic states with shorter and longer periods. (f) Chaotic solution, inset: evolution of Euclidian norm σ of perturbed and unperturbed trajectories.

recovery and thus, enable the formation of rich dynamics. The formulation of the problem via the EOM allowed us to perform a detailed bifurcation analysis for a two-pulse state without having to rely on the full model described by the Haus master equation. Intermediate checks of the EOM showed excellent quantitative agreement with the full model. We were able to identify many interesting regimes and, besides equidistant states, we observed non-equidistant configurations where one pulse is anchored by the satellite induced by another pulse. These non-equidistant states can also be multistable, as well as the coexistence of different non-equidistant states. Further, we describe periodic configurations in which the pulses oscillate around the equidistant configuration. Next, for states with more than two pulses, even more complex dynamics are possible due to the higher dimensionality of the problem. Besides more complex states with non-equidistant and periodic configurations described above, we also predict the existence of chaotic regimes. Finally, we note that in the situation where the distance between pulses gets smaller, gain repulsion becomes dominant which renders the dynamics for the relative positions very fast. This situation would allow us to perform an adiabatic elimination of these fast degrees of freedom and consider only a model for the phase of the optical pulses. This case corresponds to the model discussed in [20] where the interaction between the phases is described by a Kuramoto model with nearest neighbor interactions that follows from the EOM detailed here.

Declaration of competing interest

The authors declare that they have no known competing financial interests or personal relationships that could have appeared to influence the work reported in this paper.

Acknowledgment

We acknowledge the financial support of the project KOGIT, Agence Nationale de la Recherche (No. ANR-22-CE92-0009) and Deutsche Forschungsgemeinschaft (DFG) via Grant No. 505936983. TGS and JJ acknowledge funding from the Studienstiftung des Deutschen Volkes and the Ministerio de Economía y Competitividad (PID2021-128910NB-I00 AEI/FEDER UE, PGC2018-099637-B-I00 AEI/FEDER UE), respectively.

Data availability

Data will be made available on request.

References

- [1] H.A. Haus. Mode-locking of lasers. *IEEE J. Selected Topics Quantum Electron.*, 6(6):1173–1185, 2000. doi: 10.1109/2944.902165.
- [2] Steven T. Cundiff and Jun Ye. Colloquium: Femtosecond optical frequency combs. *Rev. Mod. Phys.*, 75:325–342, Mar 2003. doi: 10.1103/RevModPhys.75.325. URL <https://link.aps.org/doi/10.1103/RevModPhys.75.325>.
- [3] Scott A. Diddams. The evolving optical frequency comb. *J. Opt. Soc. Am. B*, 27(11):B51–B62, Nov 2010. doi: 10.1364/JOSAB.27.000B51. URL <http://josab.osa.org/abstract.cfm?URI=josab-27-11-B51>.
- [4] Alessia Pasquazi, Marco Peccianti, Luca Razzari, David J. Moss, Stephane Coen, Miro Erkintalo, Yanne K. Chembo, Tobias Hansson, Stefan Wabnitz, Pascal Del’Haye, Xiaoxiao Xue, Andrew M. Weiner, and Roberto Morandotti. Micro-combs: A novel generation of optical sources. *Physics Reports*, 729:1 – 81, 2018. ISSN 0370-1573. doi: <https://doi.org/10.1016/j.physrep.2017.08.004>. URL <http://www.sciencedirect.com/science/article/pii/S0370157317303253>.
- [5] D. Novak, Z. Ahmed, R.B. Waterhouse, and R.S. Tucker. Signal generation using pulsed semiconductor lasers for application in millimeter-wave wireless links. *Microwave Theory and Techniques, IEEE Transactions on*, 43(9):2257–2262, sep 1995. ISSN 0018-9480. doi: 10.1109/22.414573.
- [6] Masaru Kuramoto, Nobuyoshi Kitajima, Hengchang Guo, Yuji Furushima, Masao Ikeda, and Hiroyuki Yokoyama. Two-photon fluorescence bioimaging with an all-semiconductor laser picosecond pulse source. *Opt. Lett.*, 32(18):2726–2728, Sep 2007. doi: 10.1364/OL.32.002726. URL <http://ol.osa.org/abstract.cfm?URI=ol-32-18-2726>.
- [7] S. M. Link, D. J. H. C. Maas, D. Waldburger, and U. Keller. Dual-comb spectroscopy of water vapor with a free-running semiconductor disk laser. *Science*, 2017. ISSN 0036-8075. doi: 10.1126/science.aam7424. URL <http://science.sciencemag.org/content/early/2017/05/10/science.aam7424>.
- [8] U. Keller, K. J. Weingarten, F. X. Kärtner, D. Kopf, B. Braun, I. D. Jung, R. Fluck, C. Hönninger, N. Matuschek, and J. Aus der Au. Semiconductor saturable absorber mirrors (SESAM’s) for femtosecond to nanosecond pulse generation in solid-state lasers. *Selected Topics in Quantum Electronics, IEEE Journal of*, 2:435–453, 1996.
- [9] D. Lorenser, H. J. Unold, D. J. H. C. Maas, A. Aschwanden, R. Grange, R. Paschotta, D. Ebling, E. Gini, and U. Keller. Towards wafer-scale integration of high repetition rate passively mode-locked surface-emitting semiconductor lasers. *Appl. Phys. B*, 79:927–932, 2004.
- [10] Th. Udem, R. Holzwarth, and T. W. Hänsch. Optical frequency metrology. *Nature*, 416(6877):233–237, Mar 2002. ISSN 1476-4687. doi: 10.1038/416233a. URL <https://doi.org/10.1038/416233a>.
- [11] Ursula Keller. Recent developments in compact ultrafast lasers. *Nature*, 424(6950):831–838, 2003. ISSN 1476-4687. doi: 10.1038/nature01938. URL <https://doi.org/10.1038/nature01938>.
- [12] E. Avrutin and J. Javaloyes. *Mode-Locked Semiconductor Lasers, Book Chapter In: Handbook of Optoelectronic Device Modeling and Simulation*. CRC press, Taylor and Francis, United Kingdom, 2017. ISBN 9781498749381. URL <https://www.crcpress.com/Handbook-of-Optoelectronic-Device-Modeling-and-Simulation---Two-Volume/Piprek/p/book/9781498749381>.
- [13] M. Marconi, J. Javaloyes, S. Balle, and M. Giudici. How lasing localized structures evolve out of passive mode locking. *Phys. Rev. Lett.*, 112:223901, Jun 2014. doi: 10.1103/PhysRevLett.112.223901. URL <https://link.aps.org/doi/10.1103/PhysRevLett.112.223901>.
- [14] M. Marconi, J. Javaloyes, P. Camelin, D.C. Gonzalez, S. Balle, and M. Giudici. Control and generation of localized pulses in passively mode-locked semiconductor lasers. *IEEE J. Sel. Top. Quantum Electron.*, 21(6):1–10, Nov 2015. ISSN 1077-260X. doi: 10.1109/JSTQE.2015.2435895.
- [15] P. Camelin, J. Javaloyes, M. Marconi, and M. Giudici. Electrical addressing and temporal tweezing of localized pulses in passively-mode-locked semiconductor lasers. *Phys. Rev. A*, 94:063854, Dec 2016. doi: 10.1103/PhysRevA.94.063854. URL <http://link.aps.org/doi/10.1103/PhysRevA.94.063854>.
- [16] P. Camelin, C. Schelte, A. Verschelde, A. Garnache, G. Beaudoin, I. Sagnes, G. Huyet, J. Javaloyes, S. V. Gurevich, and M. Giudici. Temporal localized structures in mode-locked vertical external-cavity surface-emitting lasers. *Opt. Lett.*, 43(21):5367–5370, Nov 2018. doi: 10.1364/OL.43.005367. URL <http://ol.osa.org/abstract.cfm?URI=ol-43-21-5367>.
- [17] J.N. Kutz, B.C. Collings, K. Bergman, and W.H. Knox. Stabilized pulse spacing in soliton lasers due to gain depletion and recovery. *Quantum Electronics, IEEE Journal of*, 34(9):1749–1757, Sep 1998. ISSN 0018-9197. doi: 10.1109/3.709592.
- [18] Michel Nizette, Dmitrii Rachinskii, Andrei Vladimirov, and Matthias Wolfrum. Pulse interaction via gain and loss dynamics in passive mode locking. *Physica D: Nonlinear Phenomena*, 218(1):95 – 104, 2006. ISSN 0167-2789. doi: <http://dx.doi.org/10.1016/j.physd.2006.04.013>. URL <http://www.sciencedirect.com/science/article/pii/S0167278906001436>.
- [19] J. Javaloyes, P. Camelin, M. Marconi, and M. Giudici. Dynamics of localized structures in systems with broken parity symmetry. *Phys. Rev. Lett.*, 116:133901, Mar 2016. doi: 10.1103/PhysRevLett.116.133901. URL <http://link.aps.org/doi/10.1103/PhysRevLett.116.133901>.
- [20] T. G. Seidel, A. Bartolo, A. Garnache, M. Giudici, M. Marconi, S. V. Gurevich, and J. Javaloyes. Multistable kuramoto splay states in a crystal of mode-locked laser pulses. *Phys. Rev. Lett.*, 134:033801, Jan 2025. doi: 10.1103/PhysRevLett.134.033801. URL <https://link.aps.org/doi/10.1103/PhysRevLett.134.033801>.
- [21] Michel Fruchart, Ryo Hanai, Peter B. Littlewood, and Vincenzo Vitelli. Non-reciprocal phase transitions. *Nature*, 592(7854):363–369, Apr 2021. ISSN 1476-4687. doi: 10.1038/s41586-021-03375-9. URL <https://doi.org/10.1038/s41586-021-03375-9>.
- [22] C. Otto, Lüdge K., A. Vladimirov, M. Wolfrum, and E. Schöll. Delay induced dynamics and jitter reduction of passively mode-locked semiconductor laser subject to optical feedback. *New J. Phys.*, 14:113033, 2012.
- [23] D. Arsenijević, Kleinertm M., and Bimbergm D. Phase noise and jitter reduction by optical feedback on passively mode-locked quantum-dot lasers. *Appl. Phys. Lett.*, 103:231101, 2013.
- [24] Lina Jaurigue, Alexander Pimenov, Dmitrii Rachinskii, Eckehard Schöll, Kathy Lüdge, and Andrei G. Vladimirov. Timing jitter of passively-mode-locked semiconductor lasers subject to optical feedback: A semi-analytic approach. *Phys. Rev. A*, 92:053807, Nov 2015. doi: 10.1103/PhysRevA.92.053807. URL <https://link.aps.org/doi/10.1103/PhysRevA.92.053807>.

- [25] O. Nikiforov, L. Jaurigue, L. Drzewietzki, K. Lüdge, and S. Breuer. Experimental demonstration of change of dynamical properties of a passively mode-locked semiconductor laser subject to dual optical feedback by dual full delay-range tuning. *Opt. Express*, 24(13):14301–14310, Jun 2016. doi: 10.1364/OE.24.014301. URL <https://opg.optica.org/oe/abstract.cfm?URI=oe-24-13-14301>.
- [26] Lina Jaurigue, Bernd Krauskopf, and Kathy Lüdge. Multipulse dynamics of a passively mode-locked semiconductor laser with delayed optical feedback. *Chaos: An Interdisciplinary Journal of Nonlinear Science*, 27(11):114301, 2017. doi: 10.1063/1.5006743. URL <https://doi.org/10.1063/1.5006743>.
- [27] A. Bartolo, T. G. Seidel, N. Vigne, A. Garnache, G. Beaudoin, I. Sagnes, M. Giudici, J. Javaloyes, S. V. Gurevich, and M. Marconi. Manipulation of temporal localized structures in a vertical external-cavity surface-emitting laser with optical feedback. *Opt. Lett.*, 46(5):1109–1112, Mar 2021. doi: 10.1364/OL.414353. URL <http://ol.osa.org/abstract.cfm?URI=ol-46-5-1109>.
- [28] Thomas G. Seidel, Julien Javaloyes, and Svetlana V. Gurevich. Influence of time-delayed feedback on the dynamics of temporal localized structures in passively mode-locked semiconductor lasers. *Chaos: An Interdisciplinary Journal of Nonlinear Science*, 32(3):033102, 03 2022. ISSN 1054-1500. doi: 10.1063/5.0075449. URL <https://doi.org/10.1063/5.0075449>.
- [29] J. Javaloyes, M. Marconi, and M. Giudici. Nonlocality induces chains of nested dissipative solitons. *Phys. Rev. Lett.*, 119:033904, Jul 2017. doi: 10.1103/PhysRevLett.119.033904. URL <https://link.aps.org/doi/10.1103/PhysRevLett.119.033904>.
- [30] P. Grelu and N. Akhmediev. Dissipative solitons for mode-locked lasers. *Nat Photon*, 6(2):84–92, 2012. ISSN 1749-4885. doi: 10.1038/nphoton.2011.345. URL <http://dx.doi.org/10.1038/nphoton.2011.345>.
- [31] Xueming Liu. Interaction and motion of solitons in passively-mode-locked fiber lasers. *Phys. Rev. A*, 84:053828, Nov 2011. doi: 10.1103/PhysRevA.84.053828. URL <https://link.aps.org/doi/10.1103/PhysRevA.84.053828>.
- [32] Nail Akhmediev, Augusto S Rodrigues, and Graham E Town. Interaction of dual-frequency pulses in passively mode-locked lasers. *Optics Communications*, 187(4):419–426, 2001. ISSN 0030-4018. doi: [https://doi.org/10.1016/S0030-4018\(00\)01116-0](https://doi.org/10.1016/S0030-4018(00)01116-0). URL <https://www.sciencedirect.com/science/article/pii/S0030401800011160>.
- [33] Z. Q. Wang, K. Nithyanandan, A. Coillet, P. Tchofo-Dinda, and Ph. Grelu. Optical soliton molecular complexes in a passively mode-locked fibre laser. *Nature Communications*, 10(1):830, Feb 2019. ISSN 2041-1723. doi: 10.1038/s41467-019-08755-4. URL <https://doi.org/10.1038/s41467-019-08755-4>.
- [34] J. M. Soto-Crespo and N. N. Akhmediev. Multisoliton regime of pulse generation by lasers passively mode locked with a slow saturable absorber. *J. Opt. Soc. Am. B*, 16(4):674–677, Apr 1999. doi: 10.1364/JOSAB.16.000674. URL <https://opg.optica.org/josab/abstract.cfm?URI=josab-16-4-674>.
- [35] Alexey Kokhanovskiy, Evgeniy Kuprikov, and Sergey Kobtsev. Single- and multi-soliton generation in figure-eight mode-locked fibre laser with two active media. *Optics & Laser Technology*, 131:106422, 2020. ISSN 0030-3992. doi: <https://doi.org/10.1016/j.optlastec.2020.106422>. URL <https://www.sciencedirect.com/science/article/pii/S0030399220310550>.
- [36] Andrei G. Vladimirov. Short- and long-range temporal cavity soliton interaction in delay models of mode-locked lasers. *Phys. Rev. E*, 105:044207, Apr 2022. doi: 10.1103/PhysRevE.105.044207. URL <https://link.aps.org/doi/10.1103/PhysRevE.105.044207>.
- [37] D. Puzyrev, A. G. Vladimirov, A. Pimenov, S. V. Gurevich, and S. Yanchuk. Bound pulse trains in arrays of coupled spatially extended dynamical systems. *Phys. Rev. Lett.*, 119:163901, Oct 2017. doi: 10.1103/PhysRevLett.119.163901. URL <https://link.aps.org/doi/10.1103/PhysRevLett.119.163901>.
- [38] Andrei G. Vladimirov. Temporal cavity soliton interaction in passively mode-locked semiconductor lasers. *Optics*, 4(3):433–446, 2023. ISSN 2673-3269. doi: 10.3390/opt4030031. URL <https://www.mdpi.com/2673-3269/4/3/31>.
- [39] A. G. Vladimirov and D. Turaev. Model for passive mode locking in semiconductor lasers. *Phys. Rev. A*, 72:033808, Sep 2005. doi: 10.1103/PhysRevA.72.033808. URL <http://link.aps.org/doi/10.1103/PhysRevA.72.033808>.
- [40] Theodore Kolokolnikov, Michel Nizette, Thomas Erneux, Nicolas Joly, and Serge Bielawski. The Q -switching instability in passively mode-locked lasers. *Physica D: Nonlinear Phenomena*, 219(1):13–21, 2006. ISSN 0167-2789. doi: <https://doi.org/10.1016/j.physd.2006.05.006>. URL <http://www.sciencedirect.com/science/article/pii/S0167278906001801>.
- [41] A. M. Perego, B. Garbin, F. Gustave, S. Barland, F. Prati, and G. J. de Valcárcel. Coherent master equation for laser modelocking. *Nat. Commun.*, 11(1):311, 2020. ISSN 2041-1723. doi: 10.1038/s41467-019-14013-4.
- [42] Jan Hausen, Kathy Lüdge, Svetlana V. Gurevich, and Julien Javaloyes. How carrier memory enters the haus master equation of mode-locking. *Opt. Lett.*, 45(22):6210–6213, Nov 2020. doi: 10.1364/OL.406136. URL <http://ol.osa.org/abstract.cfm?URI=ol-45-22-6210>.
- [43] Michel Nizette and Andrei G. Vladimirov. Generalized haus master equation model for mode-locked class- b lasers. *Phys. Rev. E*, 104:014215, Jul 2021. doi: 10.1103/PhysRevE.104.014215. URL <https://link.aps.org/doi/10.1103/PhysRevE.104.014215>.
- [44] Marcel G. Clerc, Ricardo G. Elías, and René G. Rojas. Continuous description of lattice discreteness effects in front propagation. *Philosophical Transactions of the Royal Society A: Mathematical, Physical and Engineering Sciences*, 369(1935):412–424, 2011. ISSN 1364-503X. doi: 10.1098/rsta.2010.0255. URL <https://royalsocietypublishing.org/doi/full/10.1098/rsta.2010.0255>.

A. Appendix: Derivation of the Equation of Motion

In this Appendix we present the derivation of the equation of motion (EOM) starting from the Haus Master Equation (HME) Eqs. (1)-(3) of the main text.

A.1. Definitions

We define the scalar product in the vector space of real functions of periodicity T as

$$\langle w|v \rangle = \int_0^T w(z) v(z) dz.$$

In what follows we will deal with complex functions which we define as vectors with the real and imaginary parts as components. Then the scalar product reads

$$\langle w|v \rangle = \int_0^T [w_x(z) v_x(z) + w_y(z) v_y(z)] dz,$$

where the indices x, y denote the real and imaginary parts, respectively. Now considering a linear operator \mathcal{L} , one can define the adjoint operator \mathcal{L}^\dagger as

$$\langle w|\mathcal{L}v \rangle = \langle \mathcal{L}^\dagger w|v \rangle. \quad (\text{A.1})$$

As an example, we consider the operator $\mathcal{L} = i$ (multiplication with imaginary unit) it corresponds to a matrix and we have

$$\begin{aligned} i \begin{pmatrix} v_x \\ v_y \end{pmatrix} &= \begin{pmatrix} -v_y \\ v_x \end{pmatrix} \\ &= \begin{pmatrix} 0 & -1 \\ 1 & 0 \end{pmatrix} \begin{pmatrix} v_x \\ v_y \end{pmatrix}, \\ i^\dagger \begin{pmatrix} v_x \\ v_y \end{pmatrix} &= \begin{pmatrix} v_y \\ -v_x \end{pmatrix} \\ &= \begin{pmatrix} 0 & 1 \\ -1 & 0 \end{pmatrix} \begin{pmatrix} v_x \\ v_y \end{pmatrix}, \end{aligned} \quad (\text{A.2})$$

such that the scalar product is preserved

$$\langle w|\mathcal{L}v \rangle = w_x(-v_y) + w_y(v_x) \quad (\text{A.3})$$

$$\langle \mathcal{L}^\dagger w|v \rangle = (w_y) v_x + (-w_x) v_y. \quad (\text{A.4})$$

A.2. Preliminaries

We consider a nonlinear complex valued partial differential equation (PDE) with periodic boundaries of the form

$$M \partial_\xi \psi = \mathcal{L} \psi + \mathcal{N}(\psi) + \eta e^{i\Omega} M \psi(z - \tau_f). \quad (\text{A.5})$$

Here, \mathcal{L} is a linear operator, $\mathcal{N}(\psi)$ is a nonlinear function and $\eta e^{i\Omega} M \psi(x - \tau_f, s)$ a non-local term describing time-delayed feedback with the feedback delay time τ_f , feedback strength η , feedback phase Ω . Further, M is the mass matrix and $M = \text{diag}(1, 1, 0, 0)$ for the HME in question (cf. Eqs.

(1)-(3) of the main text). Furthermore, $\psi = \psi(z, \xi)$ is a four-component real-valued vector function, and z and ξ denote the fast and slow time scales which describe the evolution within one round-trip and from one round-trip to the next one, respectively. The first two components of ψ correspond to the real and imaginary parts of the electric field E and the third and fourth components are the gain g and absorber q ,

$$\psi = \begin{pmatrix} \psi_x \\ \psi_y \\ \psi_g \\ \psi_q \end{pmatrix} = \begin{pmatrix} \text{Re}(E) \\ \text{Im}(E) \\ g - g_0 \\ q - q_0 \end{pmatrix}.$$

Here, g_0 is the pumping rate and q_0 is the value of the unsaturated losses that determines the modulation depth of the saturable absorber. For convenience and to account for the explicit form of the mass matrix M , we also define the field and carrier components as two-component vector functions

$$\psi_f = (\psi_x, \psi_y, 0, 0)^T, \quad \psi_c = (0, 0, \psi_g, \psi_q)^T$$

such that $\psi = \psi_f + \psi_c$.

Next, we assume that the PDE (A.5) has a stationary single-pulse solution $\psi_s(z)$ and two neutral modes corresponding to the phase invariance (only for the field components) and translation invariance. Hence, every shifted and rotated version of ψ_s is a solution of Eq. (A.5) as well. Hence we define the one pulse solution $\psi_j = \psi_j(\xi, t)$ as

$$\begin{aligned} \psi_j &= e^{i\varphi_j(\xi)} \psi_{s,f}(z - z_j(\xi)) + \psi_{s,c}(z - z_j(\xi)) \\ &= R(\varphi_j(\xi)) \psi_s(z - z_j(\xi)), \end{aligned}$$

where $\varphi_j(\xi)$ and $x_j(\xi)$ are the phase and position of the pulse which depend on the slow time, and $\psi_{s,f}$ and $\psi_{s,c}$ are the field and carrier components of the stationary solution. Further, $R(\varphi)$ is a rotation matrix

$$R(\varphi) = \begin{pmatrix} \cos \varphi & -\sin \varphi & 0 & 0 \\ \sin \varphi & \cos \varphi & 0 & 0 \\ 0 & 0 & 1 & 0 \\ 0 & 0 & 0 & 1 \end{pmatrix}$$

for the field components. Next, we employ a superposition ansatz to describe solutions Ψ that consist of N pulses

$$\Psi = \sum_{j=1}^N \psi_j + \delta\psi, \quad (\text{A.6})$$

where $\delta\psi$ accounts for a small deviation from the simple summation. The aim of the following derivation is to determine how multiple pulses ψ_j interact in the cavity. This can be expressed as dynamical *equations of motion* for $\varphi_j(\xi)$ and $z_j(\xi)$, respectively.

A.3. Linearization

Inserting the superposition ansatz (A.6) into Eq. (A.5) yields (here the dot operators on the r.h.s. denote the derivatives with respect to slow time: ∂_ξ)

$$\begin{aligned}
M\partial_\xi\Psi &= \sum_{j=1}^N [- (M\partial_z\psi_j) \dot{z}_j + (M\partial_\phi\psi_j) \dot{\phi}_j] + \\
&\quad M\delta\dot{\psi} \\
&= \sum_{j=1}^N \mathcal{L}\psi_j + \mathcal{L}\delta\psi + \mathcal{N}\left(\sum_{j=1}^N \psi_j + \delta\psi\right) + \\
&\quad \eta MR(\Omega) \sum_{j=1}^N \psi_j (x - \tau_f) \\
&= \sum_{j=1}^N \mathcal{L}\psi_j + \mathcal{N}\left(\sum_{j=1}^N \psi_j\right) + \\
&\quad \eta MR(\Omega) \sum_{j=1}^N \psi_j (z - \tau_f) + \quad (A.7) \\
&\quad \left(\mathcal{L} + \left(\frac{\partial\mathcal{N}}{\partial\psi}\right)\Big|_{\psi=\sum_j\psi_j}\right) \delta\psi,
\end{aligned}$$

where in the last step, we expanded the nonlinearity around $\delta\psi = 0$. Further, we can identify the Jacobian defined as

$$\mathcal{J} = \mathcal{L} + \left(\frac{\partial\mathcal{N}}{\partial\psi}\right)\Big|_{\psi=\sum_j\psi_j}.$$

Around a single pulse, one of the ψ_j is dominant and governs the dynamics. Hence, the Jacobian around a pulse ψ_m is approximately

$$\mathcal{J} \approx \mathcal{J}_m = \mathcal{L} + \left(\frac{\partial\mathcal{N}}{\partial\psi}\right)\Big|_{\psi_m}.$$

Further, we can expand the nonlinearity in Eq. (A.7) around the same pulse

$$\mathcal{N}\left(\sum_{j=1}^N \psi_j\right) = \mathcal{N}(\psi_m) + \frac{\partial\mathcal{N}}{\partial\psi}\Big|_{\psi_m} \sum_{j \neq m} \psi_j$$

such that one obtains

$$\begin{aligned}
\sum_{j=1}^N \mathcal{L}\psi_j + \mathcal{N}\left(\sum_{j=1}^N \psi_j\right) &= \left(\mathcal{L} + \frac{\partial\mathcal{N}}{\partial\psi}\Big|_{\psi_m}\right) \sum_{j \neq m} \psi_j \\
&= \mathcal{J}_m \sum_{j \neq m} \psi_j,
\end{aligned}$$

where we used $\mathcal{L}\psi_m + \mathcal{N}(\psi_m) = 0$ as ψ_m solves Eq. (A.5) in the absence of the feedback term. With these shortcuts, we can rewrite Eq. (A.7) as

$$(M\partial_\xi - \mathcal{J}_m) \delta\psi = \sum_{j=1}^N M\partial_z\psi_j \dot{z}_j - M\partial_\phi\psi_j \dot{\phi}_j +$$

$$\mathcal{J}_m \sum_{j \neq m} \psi_j + \quad (A.8)$$

$$\eta MR(\Omega) \sum_{j=1}^N \psi_j (z - \tau_f)$$

which is valid around pulse ψ_m . The Jacobian \mathcal{J}_m possess eigenvalues $\lambda_i^{(m)}$ corresponding to eigenfunctions $v_i^{(m)}$ which are defined by the generalized eigenvalue problem

$$\mathcal{J}_m v_i^{(m)} = \lambda_i^{(m)} M v_i^{(m)}.$$

We know that two (neutral) eigenvalues are zero due to the rotational and translation symmetry in Eq. (A.7). The corresponding neutral eigenfunctions $v_t^{(m)}$ and $v_p^{(m)}$ read

$$v_t^{(m)} = \partial_z \psi_m \quad (A.9)$$

$$v_p^{(m)} = \partial_\phi \psi_m = i M \psi_m, \quad (A.10)$$

where the indices t, p stand for *translation* and *phase*, respectively. Note that we can also define Eqs. (A.9), (A.10) in terms of the eigenfunctions of the stationary solutions ψ_s which we simply define as v_t and v_p as $v_t^{(m)} = R(\varphi_m) v_t(z - z_m)$ and $v_p^{(m)} = R(\varphi_m) v_p(z - z_m)$. In the next step, we can now decompose $\delta\psi$ in Eq. (A.8) in the basis of eigenfunctions $v_i^{(m)}$

$$\delta\psi = \sum_j \beta_j^{(m)}(\xi) v_j^{(m)}, \quad (A.11)$$

where the $\beta_j^{(m)}(\xi)$ are the time-dependent coefficients.

Next, we consider the corresponding adjoint eigenvalue problem defined by the adjoint operator \mathcal{J}_m^\dagger which has eigenfunctions $w_i^{(m)}$ and eigenvalues that are the complex conjugated of the eigenvalues of \mathcal{J}_m , i.e.

$$\mathcal{J}_m^\dagger w_i^{(m)} = \bar{\lambda}_i^{(m)} M w_i^{(m)}$$

where we used that $M^\dagger = M$ for the HME. At this point it is instructive to clarify important properties of the eigenfunctions. First, $(v_i^{(m)}, w_i^{(m)})$ form a biorthogonal set, i.e.

$$\langle w_i^{(m)} | M v_j^{(m)} \rangle = 0, \quad \forall i \neq j. \quad (A.12)$$

This property can be easily shown when computing $\langle w_i^{(m)} | \mathcal{J}_m v_j^{(m)} \rangle$ in two ways:

$$\begin{aligned}
\langle w_i^{(m)} | \mathcal{J}_m v_j^{(m)} \rangle &= \lambda_j^{(m)} \langle w_i^{(m)} | M v_j^{(m)} \rangle, \\
\langle w_i^{(m)} | \mathcal{J}_m v_j^{(m)} \rangle &= \langle \mathcal{J}_m^\dagger w_i^{(m)} | v_j^{(m)} \rangle \\
&= \bar{\lambda}_i^{(m)} \langle M^\dagger w_i^{(m)} | v_j^{(m)} \rangle \\
&= \bar{\lambda}_i^{(m)} \langle w_i^{(m)} | M v_j^{(m)} \rangle.
\end{aligned}$$

As this must hold for all i, j , in general $\lambda_j^{(m)} \neq \bar{\lambda}_i^{(m)}$, $\forall i \neq j$ and hence $\langle w_i^{(m)} | M v_j^{(m)} \rangle = 0$. Further, as the solutions ψ_m are localized around z_m , so are the $v_i^{(m)}$ and $w_i^{(m)}$. As we assume well separated pulses, we obtain

$$\langle w_i^{(k)} | M v_j^{(m)} \rangle \approx 0, \quad \forall k \neq m, \quad \forall i, j. \quad (\text{A.13})$$

A.4. Projection on adjoint eigenmodes

We insert the expansion of $\delta\psi$ in the eigenfunctions defined in Eqs. (A.11) into (A.8) and identify the eigenfunctions defined in Eqs. (A.9), (A.10) to obtain

$$\begin{aligned} \sum_i \left(\partial_\xi - \lambda_i^{(m)} \right) \beta_i^{(m)} M v_i^{(m)} = \\ \sum_{j=1}^N \left[M v_t^{(m)} \dot{z}_j - M v_p^{(m)} \dot{\phi}_j \right] + \\ \mathcal{J}_m \sum_{j \neq m} \psi_j + \eta M R(\Omega) \sum_{j=1}^N \psi_j (z - \tau_f). \end{aligned} \quad (\text{A.14})$$

Projecting this equation onto an adjoint eigenmode $w_k^{(m)}$ corresponding to the same pulse and using the properties in Eqs. (A.12) and (A.13) yields

$$\begin{aligned} \sum_i \left(\partial_\xi - \lambda_i^{(m)} \right) \beta_i^{(m)} \langle w_k^{(m)} | M v_i^{(m)} \rangle \\ = \left(\partial_\xi - \lambda_i^{(m)} \right) \beta_k^{(m)} \langle w_k^{(m)} | M v_k^{(m)} \rangle. \end{aligned} \quad (\text{A.15})$$

Inserting this into Eq. (A.14) gives

$$\begin{aligned} \partial_\xi \beta_k^{(m)} = \lambda_i^{(m)} \beta_k^{(m)} + C_k^{(m)}, \\ \text{where } C_k^{(m)} = \frac{\langle w_k^{(m)} | \text{RHS (A.14)} \rangle}{\langle w_k^{(m)} | M v_k^{(m)} \rangle}. \end{aligned}$$

When projecting on the all eigenmodes except for $w_t^{(m)}$ and $w_p^{(m)}$, the $\beta_k^{(m)}$ will not diverge as the corresponding eigenvalues $\lambda_k^{(m)}$ are negative since ψ_m is a stable stationary solution. For $w_{t,p}^{(m)}$ we assume the $\beta_{t,p}^{(m)}$ to evolve slowly such that $\partial_\xi \beta_{t,p}^{(m)} \approx 0$. Therefore we obtain

$$0 = \langle w_k^{(m)} | \text{RHS (A.14)} \rangle.$$

Finally, we explicitly project onto $w_t^{(m)}$ and $w_p^{(m)}$ and use again the properties of the eigenfunctions defined in Eqs. (A.9), (A.10) such that we obtain the EOM for the phases and positions

$$\begin{aligned} N_t^{(m)} \dot{z}_m = \sum_{j \neq m} \langle w_t^{(m)} | \mathcal{J}_m \psi_j \rangle + \\ \eta \sum_{j=1}^N \langle w_t^{(m)} | M R(\Omega) \psi_j (z - \tau_f) \rangle, \end{aligned} \quad (\text{A.16})$$

$$\begin{aligned} N_p^{(m)} \dot{\phi}_m = \sum_{j \neq m} \langle w_p^{(m)} | \mathcal{J}_m \psi_j \rangle + \\ \eta \sum_{j=1}^N \langle w_p^{(m)} | M R(\Omega) \psi_j (z - \tau_f) \rangle, \end{aligned} \quad (\text{A.17})$$

where the normalization constants read

$$\begin{aligned} N_t^{(m)} = - \langle w_t^{(m)} | M v_t^{(m)} \rangle, \\ N_p^{(m)} = \langle w_p^{(m)} | M v_p^{(m)} \rangle. \end{aligned}$$

A.4.1. Alternative Approach using the Fredholm Alternative

In fact, we can also use the Fredholm alternative to get to this result faster. It states that for an inhomogeneous linear equation $Ax = b$, one can project onto the kernel eigenmode w of the corresponding adjoint homogeneous equation $A^\dagger w = 0$ to obtain

$$\langle w | b \rangle = \langle w | Ax \rangle = \langle A^\dagger w | x \rangle = 0.$$

Hence, we consider again Eq. (A.8) and use as before that the perturbation $\delta\psi$ evolves slowly (i.e. $\partial_\xi \delta\psi \ll 1$):

$$-\mathcal{J}_m \delta\psi = \text{RHS (A.14)}.$$

As $w_{t,p}^{(m)}$ are the kernel eigenmodes of \mathcal{J}_m^\dagger , we directly obtain

$$0 = \langle w_{t,p}^{(m)} | \text{RHS (A.14)} \rangle.$$

A.5. The explicit form of the EOM

In the next step, we want to evaluate the scalar products in Eqs. (A.16), (A.17) to find the explicit form of the EOM.

A.5.1. Non-local feedback term

First, we need to evaluate the scalar product containing the non-local term $\psi_j (z - \tau_f)$ in Eqs. (A.16), (A.17). We write the nonlocal term in terms of the stationary solution ψ_s as

$$M R(\Omega) \psi_j (z - \tau_f) = M R(\Omega + \varphi_j) \psi_s (z - z_j - \tau_f)$$

and use that we are dealing with period functions such that we can shift the argument in functions of the scalar product by z_m :

$$\begin{aligned} \langle w_{t,p}^{(m)} | M R(\Omega) \psi_j (z - \tau_f) \rangle \\ = \langle R(\gamma) w_{t,p} | M R(\Omega + \varphi_j) \psi_s (z - z_j + z_m - \tau_f) \rangle \\ = \langle R(\gamma) w_{t,p} | M R(\Omega + \varphi_j) \psi_s (z - \Delta_{jm} - \tau_f) \rangle, \end{aligned} \quad (\text{A.18})$$

where we define $\Delta_{jm} = z_j - z_m$ and γ is some rotation of the m -th adjoint eigenfunction $w_{t,p}^{(m)}$ with respect to the stationary state eigenfunction $w_{t,p}$. Next, we also consider the normalization factors $N_{t,p}^{(m)}$ on the l.h.s. of Eqs. (A.16), (A.17)

which depend on the eigenfunctions $v_{t,p}^{(m)}$ of the m -th pulse but can be shifted to depend only on the stationary modes $v_{t,p}$:

$$\langle w_{t,p}^{(m)} | M v_{t,p}^{(m)} \rangle = \langle R(\gamma) w_{t,p} | M R(\varphi_m) v_{t,p} \rangle. \quad (\text{A.19})$$

For solving Eqs. (A.16), (A.17) for z_m and φ_m , one needs to divide the expression in Eq. (A.18) with Eq. (A.19). We can multiply the ket-vectors with $R(-\varphi_m)$ and bra-vectors with $R(-\gamma)$ to remove the phase dependence from the denominator:

$$\begin{aligned} & \frac{\langle R(\gamma) w_{t,p} | M R(\Omega + \varphi_j) \psi_s(z - \Delta_{jm} - \tau_f) \rangle}{\langle R(\gamma) w_{t,p} | M R(\varphi_m) v_{t,p} \rangle} \\ &= \frac{\langle w_{t,p} | M R(\Omega + \theta_{jm}) \psi_s(z - \Delta_{jm} - \tau_f) \rangle}{\langle w_{t,p} | M v_{t,p} \rangle}, \end{aligned} \quad (\text{A.20})$$

where we define the phase difference $\theta_{jm} = \varphi_j - \varphi_m$. Next, we consider the action of the rotation operator $R(\alpha)$ which acts as

$$M R(\alpha) \psi_s(z) = [\cos(\alpha) + i \sin(\alpha)] \psi_{s,f}(z),$$

where the imaginary unit i can be understood as the operator defined in Eq. (A.2). Plugging this into the r.h.s. of Eq. (A.20) gives

$$\begin{aligned} & \langle w_{t,p} | M R(\Omega + \theta_{jm}) \psi_s(z - \Delta_{jm} - \tau_f) \rangle = \\ & \cos(\Omega + \theta_{jm}) \langle w_{t,p} | \psi_{s,f}(z - \Delta_{jm} - \tau_f) \rangle + \\ & \sin(\Omega + \theta_{jm}) \langle w_{t,p} | i \psi_{s,f}(z - \Delta_{jm} - \tau_f) \rangle. \end{aligned} \quad (\text{A.21})$$

We write out the scalar products explicitly (here the index i denotes p or t , respectively) and assign names to them:

$$\begin{aligned} l_{1,i}(\Delta_{jm}) &= \langle w_i | \psi_{s,f}(z - \Delta_{jm}) \rangle \\ &= \int [w_{i,x} \psi_{s,x}(z - \Delta_{jm}) + \\ & \quad w_{i,y} \psi_{s,y}(z - \Delta_{jm})] dz, \end{aligned} \quad (\text{A.22})$$

$$\begin{aligned} l_{2,i}(\Delta_{jm}) &= \langle w_i | i \psi_{s,f}(z - \Delta_{jm}) \rangle \\ &= \int [-w_{i,x} \psi_{s,y}(z - \Delta_{jm}) + \\ & \quad w_{i,y} \psi_{s,x}(z - \Delta_{jm})] dz, \end{aligned} \quad (\text{A.23})$$

$$\Rightarrow l_i(\Delta_{jm}) = \sqrt{l_{1,i}^2(\Delta_{jm}) + l_{2,i}^2(\Delta_{jm})}. \quad (\text{A.24})$$

Further, we define a phase u_i as

$$u_i = \arctan\left(\frac{l_{1,i}}{l_{2,i}}\right), \quad (\text{A.25})$$

$$\text{such that } \sin(u_i) = \frac{l_{1,i}}{l_i}, \quad \cos(u_i) = \frac{l_{2,i}}{l_i}.$$

With all these shortcuts, we rewrite Eq. (A.21) to obtain

$$\begin{aligned} & \langle w_{t,p} | M R(\Omega + \theta_{jm}) \psi_s(z - \Delta_{jm} - \tau_f) \rangle \\ &= l_{t,p}(\tau_f + \Delta_{jm}) \sin[\Omega + \theta_{jm} + u_{t,p}(\tau_f + \Delta_{jm})]. \end{aligned} \quad (\text{A.26})$$

A.5.2. Tail terms

Next, we evaluate the remaining terms in Eqs. (A.16),(A.17). First, we express all modes in terms of the stationary modes and separate into field and carrier components using $\psi_s = \psi_{s,f} + \psi_{s,c}$:

$$\begin{aligned} & \frac{\langle w_{t,p}^{(m)} | \mathcal{J}_m \psi_j \rangle}{\langle w_{t,p}^{(m)} | M v_{t,p}^{(m)} \rangle} = \frac{\langle w_{t,p} | \mathcal{J}_s R(\theta_{jm}) \psi_{s,f}(z - \Delta_{jm}) \rangle}{\langle w_{t,p} | M v_{t,p} \rangle} + \\ & \frac{\langle w_{t,p} | \mathcal{J}_s \psi_{s,c}(z - \Delta_{jm}) \rangle}{\langle w_{t,p} | M v_{t,p} \rangle}, \end{aligned}$$

where \mathcal{J}_s is the Jacobian evaluated at the stationary solution. Here, we can already identify the phase-independent term

$$b_{t,p}(\Delta_{jm}) = \langle w_{t,p} | \mathcal{J}_s \psi_{s,c}(z - \Delta_{jm}) \rangle \quad (\text{A.27})$$

from the main text. In fact, we can compute this force analytically (cf. Sec. A.7). The phase dependent term can be handled analogously to the non-local term (cf. Sec. A.5.1):

$$\begin{aligned} & \langle w_{t,p} | \mathcal{J}_s R(\theta_{jm}) \psi_{s,f}(z - \Delta_{jm}) \rangle = \\ & \cos(\theta_{jm}) \langle w_{t,p} | \mathcal{J}_s \psi_{s,f}(z - \Delta_{jm}) \rangle + \\ & \sin(\theta_{jm}) \langle w_{t,p} | \mathcal{J}_s i \psi_{s,f}(z - \Delta_{jm}) \rangle. \end{aligned} \quad (\text{A.28})$$

Again, we assign names to the integrals

$$\begin{aligned} a_{i,1}(\Delta_{jm}) &= \langle w_i | \mathcal{J}_s \psi_{s,f}(z - \Delta_{jm}) \rangle, \\ a_{i,2}(\Delta_{jm}) &= \langle w_i | \mathcal{J}_s i \psi_{s,f}(z - \Delta_{jm}) \rangle, \\ a_i(\Delta_{jm}) &= \sqrt{a_{1,i}^2(\Delta_{jm}) + a_{2,i}^2(\Delta_{jm})} \end{aligned}$$

and the corresponding phase

$$\begin{aligned} r_i &= \arctan\left(\frac{r_{1,i}}{r_{2,i}}\right), \\ \text{such that } \sin(r_i) &= \frac{a_{1,i}}{a_i}, \quad \cos(r_i) = \frac{a_{2,i}}{a_i}, \end{aligned}$$

such that we can write Eq. (A.28) as

$$\langle w_{t,p} | \mathcal{J}_s R(\theta_{jm}) \psi_{s,f}(z - \Delta_{jm}) \rangle = a_{t,p}(\Delta_{jm}) \sin[\theta_{jm} + r_{t,p}(\Delta_{jm})]. \quad (\text{A.29})$$

A.5.3. Equations of motion

Finally, we can combine the results from the previous sections (importantly Eqs. (A.26), (A.27) and (A.29)) to obtain the EOM:

$$\begin{aligned} \dot{z}_m &= \sum_{j \neq m} [A_t(\Delta_{jm}) \sin[\theta_{jm} + r_t(\Delta_{jm})] + B_t(\Delta_{jm}) + \\ & \quad L_t(\tau_f + \Delta_{jm}) \sin[\Omega + \theta_{jm} + u_t(\tau_f + \Delta_{jm})]], \end{aligned} \quad (\text{A.30})$$

$$\begin{aligned} \dot{\varphi}_m &= \sum_{j \neq m} [A_p(\Delta_{jm}) \sin[\theta_{jm} + r_p(\Delta_{jm})] + B_p(\Delta_{jm}) + \\ & \quad L_p(\tau_f + \Delta_{jm}) \sin[\Omega + \theta_{jm} + u_p(\tau_f + \Delta_{jm})]], \end{aligned} \quad (\text{A.31})$$

$$\sin \left[\Omega + \varphi_{m-1} - \varphi_m + u_p (\tau_f + z_{m-1} - z_m) \right].$$

where the capital letters stand for the normalized forces

$$A_{t,p} = \frac{a_{t,p}}{N_{t,p}}, \quad L_{t,p} = \frac{l_{t,p}}{N_{t,p}}, \quad B_{t,p} = \frac{b_{t,p}}{N_{t,p}}$$

with the normalization factors

$$N_t = -\langle w_t | M v_t \rangle, \quad N_p = \langle w_p | M v_p \rangle. \quad (\text{A.32})$$

All terms in Eqs.(A.30),(A.31) can be understood intuitively: $A_{t,p}$ are the amplitudes of the phase-dependent force (tail interaction), $B_{t,p}$ is the amplitude of the phase-independent force (interaction via carriers) and $L_{p,t}$ are the amplitude of the force stemming from the (phase-dependent) time-delayed feedback.

A.6. Special cases and simplifications

Next, we consider certain special cases and simplifications of Eqs. (A.30), (A.31).

A.6.1. Nearest neighbor interactions

First, due to exponentially decaying tails it is sufficient to consider only nearest neighbor interactions, i.e. the sum $\sum_{j \neq m}$ reduces to $j = m \pm 1$. However, while the interaction via time-delayed feedback is only with a single other pulse (for a single time delay), the interaction must not necessarily be with the nearest neighbor but depends on the relation of the time-delay τ and the length of the feedback loop τ_f , i.e. $j = \lfloor \frac{\tau_f}{\tau} N \rfloor$ (or $j = \lceil \frac{\tau_f}{\tau} N \rceil$, depending on what is closer). This enables interesting scenarios, as one can create a quasi 2D system by a proper choice of τ_f , where pulses are coupled in one dimension via overlapping tails and in the other dimension via time-delayed feedback. However, here we remain with nearest neighbor interaction and choose τ_f in the vicinity of $\frac{\tau}{N}$ such that $j = m - 1$,

$$\begin{aligned} \dot{z}_m = & A_t (z_{m+1} - z_m) \times \\ & \sin [\varphi_{m+1} - \varphi_m + r_t (z_{m+1} - z_m)] + \\ & B_t (z_{m+1} - z_m) + \\ & A_t (z_{m-1} - z_m) \times \\ & \sin [\varphi_{m-1} - \varphi_m + r_t (z_{m+1} - z_m)] + \\ & B_t (z_{m-1} - z_m) + \\ & L_t (\tau_f + z_{m-1} - z_m) \times \\ & \sin [\Omega + \varphi_{m-1} - \varphi_m + u_t (\tau_f + z_{m-1} - z_m)], \end{aligned} \quad (\text{A.33})$$

$$\begin{aligned} \dot{\varphi}_m = & A_p (z_{m+1} - z_m) \times \\ & \sin [\varphi_{m+1} - \varphi_m + r_p (z_{m+1} - z_m)] + \\ & B_p (z_{m+1} - z_m) + \\ & A_p (z_{m-1} - z_m) \times \\ & \sin [\varphi_{m-1} - \varphi_m + r_p (z_{m+1} - z_m)] + \\ & B_p (z_{m-1} - z_m) + \\ & L_p (\tau_f + z_{m-1} - z_m) \times \end{aligned} \quad (\text{A.34})$$

In this context, we need to define the boundary conditions (i.e., what does φ_{N+1} , z_{N+1} , φ_0 and z_0 mean). For the positions we need to be careful and add/subtract τ , i.e.,

$$\begin{aligned} z_{N+1} &= z_1 + \tau, \quad z_0 = z_N - \tau, \\ \varphi_{N+1} &= \varphi_1, \quad \varphi_0 = \varphi_N. \end{aligned}$$

A.6.2. Damped translational mode

Depending on the cavity geometry, the dynamics of the phases and positions can occur on different time-scales. In particular, in short cavities, interaction via carriers, namely repulsion via gain, is dominant, such that the translational mode is damped and the pulses are in an equidistant configuration $z_m - z_{m-1} = \frac{\tau}{N} \forall m$. Hence, the coefficients of the phase-dependent terms and the phase r_p in Eqs. (A.30), (A.31) become constants:

$$\begin{aligned} A_+ &= A_p \left(-\frac{\tau}{N} \right), \quad A_- = A_p \left(\frac{\tau}{N} \right) \\ r_+ &= r_p \left(-\frac{\tau}{N} \right), \quad r_- = r_p \left(\frac{\tau}{N} \right). \end{aligned}$$

Inserting these relations in Eqs. (A.33), (A.34) and neglecting the effects of time-delayed feedback for a moment, we obtain a set of Kuramoto equations for the phase interaction:

$$\begin{aligned} \dot{\varphi}_m = & A_+ \sin (\varphi_{m-1} - \varphi_m + r_+) + \\ & A_- \sin (\varphi_{m+1} - \varphi_m + r_-) + \omega_0, \end{aligned} \quad (\text{A.35})$$

where

$$\omega_0 = B_p \left(-\frac{\tau}{N} \right) + B_p \left(\frac{\tau}{N} \right)$$

is a common phase rotation that can be scaled out by using a comoving reference frame.

On the other hand, when the effects of time-delayed feedback are dominant, we obtain

$$\begin{aligned} \dot{\varphi}_m = & \eta L_p \left(\tau_f - \frac{\tau}{N} \right) \times \\ & \sin \left[\Omega + \varphi_{m-1} - \varphi_m + u_p \left(\tau_f - \frac{\tau}{N} \right) \right]. \end{aligned} \quad (\text{A.36})$$

An interesting special case occurs when choosing resonant feedback, i.e. $\tau_f = \frac{\tau}{N}$. First, we notice, that the normalization factor N_p defined in Eq. (A.32) is equal to the overlap integral $l_{2,p}(0)$ (cf. Eq. (A.23)). Consequently, we find

$$L_p(0) = \frac{l_p(0)}{l_{2,p}(0)} = \frac{1}{\cos u},$$

where we used Eq. (A.25) and defined $u = u_p(0)$. This leads to an effective EOM with a single free parameter u :

$$\dot{\varphi}_m = \frac{\eta}{\cos u} \sin (\Omega + \varphi_{m-1} - \varphi_m + u). \quad (\text{A.37})$$

A.6.3. Interaction of two pulses

The situation with only two pulses is special because right and left interaction go to the same pulse. Here we define $\theta = \varphi_2 - \varphi_1$ and $\Delta = z_2 - z_1$ as the corresponding phase and position difference, respectively,

$$\begin{aligned} \dot{\Delta} = & A_t(-\Delta) \sin[-\theta + r_t(-\Delta)] + B_t(-\Delta) + \\ & L_t(\tau_f - \Delta) \sin[\Omega - \theta + u_t(\tau_f - \Delta)] - \\ & A_t(\Delta) \sin[\theta + r_t(\Delta)] - B_t(\Delta) - \end{aligned} \quad (\text{A.38})$$

$$\begin{aligned} \dot{\theta} = & A_p(-\Delta) \sin[-\theta + r_p(-\Delta)] + B_p(-\Delta) + \\ & L_p(\tau_f - \Delta) \sin[\Omega - \theta + u_p(\tau_f - \Delta)] - \\ & A_p(\Delta) \sin[\theta + r_p(\Delta)] - B_p(\Delta) - \\ & L_p(\tau_f + \Delta) \sin[\Omega + \theta + u_p(\tau_f + \Delta)]. \end{aligned} \quad (\text{A.39})$$

Here, we note that the forces are periodic functions, i.e. $A_{p,t}(-\Delta) = A_{p,t}(\tau - \Delta)$. From Eqs. (A.38), (A.39), it is easy to see that the equations are antisymmetric in θ and Δ , i.e. we have

$$\begin{aligned} \dot{\Delta}(\Delta, \theta) &= -\dot{\Delta}(-\Delta, -\theta), \\ \dot{\theta}(\Delta, \theta) &= -\dot{\theta}(-\Delta, -\theta). \end{aligned}$$

This symmetry corresponds to the permutation of the pulses. Now, we can immediately identify two steady state $(\Delta^*, \theta^*) = (\frac{\tau}{2}, 0)$ and $(\Delta^*, \theta^*) = (\frac{\tau}{2}, \pi)$ corresponding to a symmetric configuration. However, the more interesting symmetry is the one around the steady states at $\frac{\tau}{2}$. Therefore, we consider $\Delta = \frac{\tau}{2} \pm \delta$ and $\theta = \pi \pm \alpha$ to obtain

$$\begin{aligned} \dot{\Delta}\left(\frac{\tau}{2} - \delta, \pi - \alpha\right) &= -\dot{\Delta}\left(\frac{\tau}{2} + \delta, \pi + \alpha\right), \\ \dot{\theta}\left(\frac{\tau}{2} - \delta, \pi - \alpha\right) &= -\dot{\theta}\left(\frac{\tau}{2} + \delta, \pi + \alpha\right). \end{aligned}$$

A.6.4. Linear stability analysis of N equidistant pulses

In the absence of time-delayed feedback, we can consider a set of N pulses which interact solely via gain repulsion in a unidirectional way (left to right), i.e.

$$\dot{z}_n = B_t(z_{n-1} - z_n)$$

with the boundary conditions $z_0 = z_N - \tau$ and $z_{N+1} = z_1 + \tau$. The stable steady state is the equidistant configuration $z_n^* = n\frac{\tau}{N} + v_0\xi$, where $v_0 = B_t(-\tau/N)$. To analyze its linear stability, we consider $z_n = z_n^* + \delta_n$. Then one obtains

$$\dot{\delta}_n = B_t'\left(-\frac{\tau}{N}\right)(\delta_{n-1} - \delta_n)$$

with the periodic boundary condition $\delta_0 = \delta_N$ and $\delta_{N+1} = \delta_1$. We expand the perturbations in Fourier modes

$$\delta_n = \sum_p a_p e^{\lambda_p \xi + i q_p n},$$

where due to boundary conditions, the wave number satisfies

$$e^{i q_p N} \stackrel{!}{=} 1$$

$$\Leftrightarrow q_p = \frac{2\pi}{N} p, \quad p = 0, \dots, N-1.$$

Using this expansion in Eq. (??) yields

$$\sum_p a_p \lambda_p e^{\lambda_p \xi + i q_p n} = B_t'\left(-\frac{\tau}{N}\right) \sum_p a_p e^{\lambda_p \xi + i q_p n} [e^{-i q_p} - 1].$$

This has to be fulfilled for each element of the sum individually because the modes are linearly independent. Therefore, we find

$$\begin{aligned} \lambda_p &= B_t'\left(-\frac{\tau}{N}\right) (e^{-i q_p} - 1) \\ &= B_t'\left(-\frac{\tau}{N}\right) [(\cos(q_p) - 1) - i \sin(q_p)]. \end{aligned}$$

We know that $B_t(\Delta)$ is exponentially recovering with Δ (cf. Sec. A.7) so its derivative is positive: $B_t'(-\tau/N) > 0$. Hence, we see that the steady states is indeed stable as $\cos(q_p) - 1 \leq 0 \forall p$. However, the imaginary part does not vanish for $N > 2$ and therefore leads to a convergence to the steady states in spirals. Calculating the eigenvalues explicitly yields:

- For $N = 2$ we have $q_p = \pi p$. The corresponding eigenvalues are:

$$\begin{aligned} \lambda_0 &= 0, \\ \lambda_1 &= -2B_t'\left(-\frac{\tau}{N}\right). \end{aligned}$$

- For $N = 3$ we have $q_p = \frac{2\pi}{3} p$. The corresponding eigenvalues read:

$$\begin{aligned} \lambda_0 &= 0, \\ \lambda_1 &= B_t'\left(-\frac{\tau}{N}\right) \left[-\frac{3}{2} + i \frac{\sqrt{3}}{2}\right], \\ \lambda_2 &= B_t'\left(-\frac{\tau}{N}\right) \left[-\frac{3}{2} - i \frac{\sqrt{3}}{2}\right]. \end{aligned}$$

A.7. Analytical approaches to carrier interaction

We want to characterize the interaction forces further. In particular, the phase-independent force reads

$$B_{t,p}(\Delta) = \frac{1}{N_{t,p}} \langle w_{t,p} | \mathcal{J}_s \psi_{s,c}(z - \Delta) \rangle.$$

As $\Gamma \ll 1$ (here the 1 stand representative for the absorber recovery time as this quantity is normalized), we can neglect the effect of the saturable absorber and only consider the impact of the gain. We define z_0 as the position where the pulse has decayed sufficiently such that one can assume exponential recovery. For $z > z_0$ the gain recovers as

$$\begin{aligned} \psi_{s,g}(z) &= (g_s - g_0) e^{-\Gamma(z-z_0)} = T e^{-\Gamma z}, \\ \text{where } T &= (g(z_0) - g_0) e^{\Gamma z_0}. \end{aligned}$$

We remember that this function is τ periodic. Hence, for $z < z_0$ the gain component reads

$$\psi_{s,g}(z) = (T e^{-\Gamma\tau}) e^{-\Gamma z}.$$

That is, in total one obtains

$$\psi_{s,g}(z) = T \begin{cases} e^{-\Gamma z} & z > z_0, \\ e^{-\Gamma(z+\tau)} & z < z_0. \end{cases}$$

With that in mind one can find $\psi_{s,g}(z - \Delta)$. It reads

$$\psi_{s,g}(z - \Delta) = T e^{\Gamma\Delta} \begin{cases} e^{-\Gamma z} & z > z_0 + \Delta, \\ e^{-\Gamma(z+\tau)} & z < z_0 + \Delta. \end{cases}$$

However, we remember that for the overlap integrals we integrate over $[z_p - a, z_p + a]$, where $a \ll \tau$ (because the Jacobian is a local linear approximation) and $z_p < z_0$ is the position of the pulse. As long as $\Delta > a$ (as should be the case for well-separated pulses), we can use

$$\psi_{s,g}(z - \Delta) = T e^{\Gamma\Delta} e^{-\Gamma(z+\tau)}.$$

Hence, we can calculate the force

$$B_{i,p}(\Delta) = C_{i,p} e^{\Gamma\Delta}, \quad (\text{A.40})$$

where $C_{i,p} = \frac{T}{N_{i,p}} \langle w_{i,p} | \mathcal{J}_s (e^{-\Gamma(z+\tau)} e_g) \rangle$.

Here, e_g is a unit vector with a component in the gain part.

B. Appendix: Numerical Scheme for Integrating the Haus Master Equation

For the time simulation of the Haus master equation (1)-(3), we use a split-step semi-implicit method. That is, we compute nonlinearities in the original space while the linear operators are computed using spectral methods in the frequency space. Further, we need to integrate the carriers equations separately from the field because the carriers in Eqs. (2),(3) do not contain a temporal derivative.

We consider the equation for the gain in Eq. (2) that is the following ODE

$$\partial_z g(z) = \Gamma_g g_0 - P'(z) g(z) \quad (\text{B.1})$$

where we define

$$P(z) = \int_0^z \left(\Gamma_g + |E(z')|^2 \right) dz'. \quad (\text{B.2})$$

Here, we first compute the cumulative intensity

$$I_c(z) = \int_0^z I(z') dz' \quad (\text{B.3})$$

such that $P(z) = \Gamma_g z + I_c(z)$. The integral for $I_c(z)$ can be obtained using, e.g., the trapezoid method. Equation (B.1)

can be solved using the method of integrating factors. The general solution reads

$$g(z) = e^{-P(z)} \left(g(0) + \Gamma_g g_0 \int_0^z e^{P(z')} dz' \right). \quad (\text{B.4})$$

Now, we apply the periodic boundary conditions, i.e., we set $g(0) = g(\tau)$ and solve for $g(0)$:

$$g(0) = \Gamma_g g_0 \frac{\int_0^\tau e^{P(z')} dz'}{e^{P(\tau)} - 1}. \quad (\text{B.5})$$

With that, we can update the carrier using the analytical expression in Eq. (B.4). The steps to obtain the updated absorber q are similar.

Now for the field E , we denote with E_i^j the i -th point in slow time ξ and the j -th point in fast time z . We need to integrate

$$\partial_\xi E = (\mathcal{L} + M) E, \quad (\text{B.6})$$

$$\text{where } \mathcal{L} = v \partial_z + \frac{1}{2\gamma^2} \partial_z^2 + \eta e^{i\Omega} S_{-\tau_f}, \quad (\text{B.7})$$

$$M = -k + \frac{1 - i\alpha_g}{2} g - \frac{1 - i\alpha_q}{2} q + i\omega, \quad (\text{B.8})$$

where $S_\tau = e^{\tau \partial_z}$ is the shift operator, v is the drift velocity and ω is the carrier frequency. We first make an explicit half-step in time

$$E_{i+\frac{1}{2}}^j = \left(1 + \frac{\Delta t}{2} M \right) E_i^j. \quad (\text{B.9})$$

Then, we apply the linear operator (which is done in Fourier space to handle the spatial derivatives)

$$\tilde{E}_{i+\frac{1}{2}}^j = e^{\Delta t \mathcal{L}} E_{i+\frac{1}{2}}^j = \mathcal{F}^{-1} \left[e^{\Delta t \hat{\mathcal{L}}} \mathcal{F} \left[E_{i+\frac{1}{2}}^j \right] \right]. \quad (\text{B.10})$$

Further, we make an implicit half-step to obtain E_{i+1}^j :

$$E_{i+1}^j = \frac{\tilde{E}_{i+\frac{1}{2}}^j}{1 - \frac{\Delta t}{2} M}. \quad (\text{B.11})$$

Finally, we consider v and ω . While these quantities can be scaled out of the equation, we need to find them in order to arrive at a steady state. While at the beginning of a simulation, these are additional free parameters, they can be found in a time simulation using a control loop. For the drift v , we expand

$$I_i(z) = I_{i+1}(z + v\Delta t) \quad (\text{B.12})$$

$$= I_{i+1}(z) + \frac{dI_{i+1}}{dz} v\Delta t, \quad (\text{B.13})$$

where $\frac{dI_{i+1}}{dz} = 2\text{Re} \left(E^* \frac{dE}{dz} \right)$. Now we weight both sides of the equation additionally with $\frac{dI_{i+1}}{dz}$ to take the tilt of the

intensity profile into account. We integrate over z and solve for v :

$$v = \frac{1}{\Delta t} \frac{\int_0^\tau (I_i(z) - I_{i+1}(z)) \frac{dI_{i+1}}{dz} dz}{\int_0^\tau \left(\frac{dI_{i+1}}{dz}\right)^2 dz}. \quad (\text{B.14})$$

For the carrier frequency ω , we first find the phase difference as

$$\phi_{i+1} - \phi_i = \arg(E_{i+1} E_i^*). \quad (\text{B.15})$$

But we do not simply want to sum this up because we want to the pulse itself to have a higher influence. Therefore, we have

$$\omega = \frac{1}{\Delta t} \frac{\int_0^\tau \arg(E_{i+1} E_i^*) I_{i+1} dz}{\int_0^\tau I_{i+1} dz}. \quad (\text{B.16})$$

Both equations for v and ω can be understood as corrections to an already existing drift and carrier frequency, that is, they are rather Δv and $\Delta \omega$ because E_i was already computed with some v_i and ω_i such that the updated quantities are $v_{i+1} = v_i + \Delta v$ and $\omega_{i+1} = \omega_i + \Delta \omega$, respectively.